CONSEIL EUROPÉEN POUR LA RECHERCHE NUCLÉAIRE

UNIVERSITAT POLITÈCNICA DE CATALUNYA

Characterization and optimization of CERN Secondary Emission Monitors (SEM) used for beam diagnostics.

BACHELOR DEGREE IN PHYSICS ENGINEERING
FINAL DEGREE PROJECT

by
Araceli Navarro Fernández

Supervisors:

Dr. Federico Roncarolo	CERN, Genève
Dr. Jordi Llorca	UPC, Barcelona

May 2017

Abstract

The European Organization for Nuclear Research, more commonly known as CERN, is one of the world's most influential particle physics center. The organization is based in a northwest suburb of Geneva, on the Franco-Swiss border and has 22 member states. At CERN, people with different backgrounds from all around the world work together in order to understand, among other things, the fundamental structure of the universe. To do that, particles have to be accelerated up to extremely high energies in a controlled and safe way.

This work has been carried out within the BE-BI-PM section, responsible of the beam diagnostics instruments that allow the observation of the transverse profiles of particle beams. Different instruments and techniques are used for this purpose but in the following pages only the monitors based on Secondary Electron Emission (SEE) phenomena will be tackled. After introducing the physics behind Secondary Emission Monitors (SEM), their performance and limitations will be discussed. This will be based on simulations and beam experiments performed during the thesis work, mostly related to the LINAC4 , a new linear accelerator just completed at CERN.

The first part of this document contains an introduction to the CERN accelerator chain, with particular emphasis on LINAC4 .

Chapter 2 focuses on various aspects of the particles interaction with matter, which are used to define the theory behind SEE, the main process behind the SEM's signal generation.

Chapter 3 starts presenting some examples of SEM detectors, focusing on SEM grids and Wire Scanners. This is followed with a practical example in which SEM grids were used in order to understand the flawed Beam Current Transformers (BCT) measurement of the beam transmission along the linac.

Chapter 4 explains the theory defining the thermal impact of particles interacting with matter. Such a theory was used to simulate the heating of SEMs during their operation.

Chapter 5 introduces the concept of beam emittance and how SE detectors can be used for its estimation. This explanation is again presented with a practical example of emittance measurement in the LINAC4 3 MeV Test Stand. Chapter 6 gives some insights on the physics behind electron stripping and CFI injection, followed with the description of the stripping system that will be installed at the exit of LINAC4 in order to inject protons into the Proton Synchrotron Booster (PSB). The main part of this chapter will present the experimental results of a series of experiments performed at the LINAC4 Half Sector Test (HST) facility by means of the H^0/H^- monitors.

Contents

Chapter 1

Introduction

CERN Accelerator Complex

The CERN accelerator complex consists in a succession of many different types of linear and circular accelerators and interconnecting transfer lines that allow particles to achieve high energies. Each machine boosts the energy of the bean of particles before injecting them to the next machine in the sequence. In Fig. 1 we can see a scheme of the complex that culminates with the Large Hadron Collider (LHC), a 27 km tunnel where particle beams are accelerated up to the record energy of 6.5 TeV per beam.

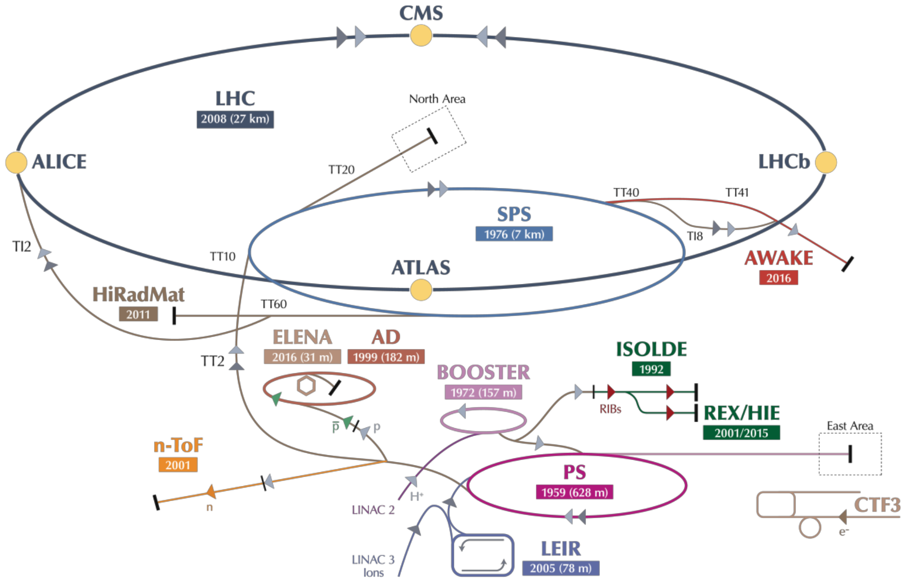

Figure 1: CERN Accelerator Complex

At the beginning of the chain the protons are generated by a source, which consists in a bottle of hydrogen. After electron stripping by high electric fields, the resulting protons are extracted towards the first accelerator, LINAC2. This accelerator, about 80 m long, brings the particles up to an energy of 50 MeV.

The protons are then transferred to the Proton Synchroton Booster (PSB) where they are accelerated up to 1.4 GeV and afterwards they are sent to the Proton Synchrotron (PS). The PS is a 628 m in circumference and the particles reach a 99.9 of the speed of light.

After reaching 26 GeV in the PS, the protons are injected in the Super Proton Synchrotron (SPS) and accelerated up to 450 GeV. Finally, they are transferred to the two LHC rings. In one of the rings particles circulate clockwise whereas in the other they circulate anticlockwise. The counter rotating rings cross over in the four detector cabins (ALICE, ATLAS, CMS, LHCb) where particles collide.

The complex of the CERN accelerator is very versatile and far from being just the injectors of the LHC. Some of the machines have their own dedicated experimental areas to explore a wide range of physics phenomena. The complexity of these machines and experimental areas makes it impossible to explain all of them.

In the following section we are going to give some insights of LINAC4 , which has been the context of all our simulations and measurements. LINAC4 was conceived to replace the old LINAC2. Its construction and commissioning up to its to energy of 160 MeV were completed at the beginning of 2017 and its connection to the PSB is foreseen for 2019.

LINAC4 Project

The source and the linac are essential for determining the LHC beams quality, since they determine the maximum beam *brilliance*, which can be seen as the maximum density of particles that can be brought into collision in a collider. Such a brilliance, that after the linac can only be deteriorated and not increased, is achieved by find the right compromise between maximum beam intensity and minimum transverse/longitudinal beam dimensions.
More than 10 years ago, in order to address the LINAC2 ageing and to improve the beam brilliance, it was decided to design and build Ł4, an H^- linear accelerator, able to accelerate pulses of up to 10^{14} particles to 160 MeV.

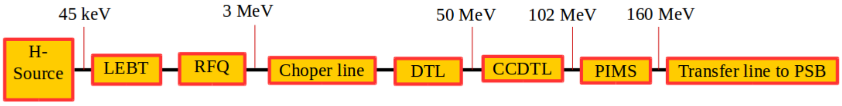

Figure 2: LINAC4 schematic layout

The LINAC4 layout is shown in Fig. 2. The chosen sequence of accelerating sections is quite standard for modern pulsed linac designs. The particles are produced in the ions source which is followed by a Low Energy Beam Transport (LEBT), needed to match the beam with the Radio Frequency Quadruple (RFQ) cavitiy. The RFQ is followed by a chopping line and a sequence of three accelerating structures. These three structures bring the energy up to 160 MeV and they are a Drift Tube Linac (DTL), a Cell-Coupled Drift Tube Linac (CCDTL) and a Pi-Mode Structure (PIMS). They increase the particles' energy up to 50 MeV, 100 MeV and 160 MeV respectively. More details can be found in [1].

Along the 86 m of the new linear accelerator, a considerable amount of detectors are installed in order to monitor and control the beam. In the following pages we will focus on the transverse beam profile and emittance monitors, giving special attention to the SEM grids and Wire scanners (Chapter 3) and slit-grid system (Chapter 5). More details about all the other LINAC4 beam diagnostics can be found in [1].

Chapter 2

Interaction of particles with matter

When a particle propagates through matter, it will have certain probability to interact with the nuclei or with the electrons present in that material. The probability that the particles have of interacting with the medium, either with the electrons or the nucleus, is represented by what is called the cross sections. The total interaction cross section will be the sum of the cross sections of the individual possible interactions. As we can see in Fig. 3, when a charged particle travels through matter it predominantly interacts with the electrons of the medium, either by Coulomb force interactions or collision interactions. Interactions with the core of the nucleus are also possible (i.e. Rutherford scattering) but much less frequent. In the following chapter we shall focus our analysis on non-relativistic or near relativistic ions interacting with solid targets. Due to the range of energy we will be working on, we are going to focus in the interactions that an incident ion has with the electrons in the medium.

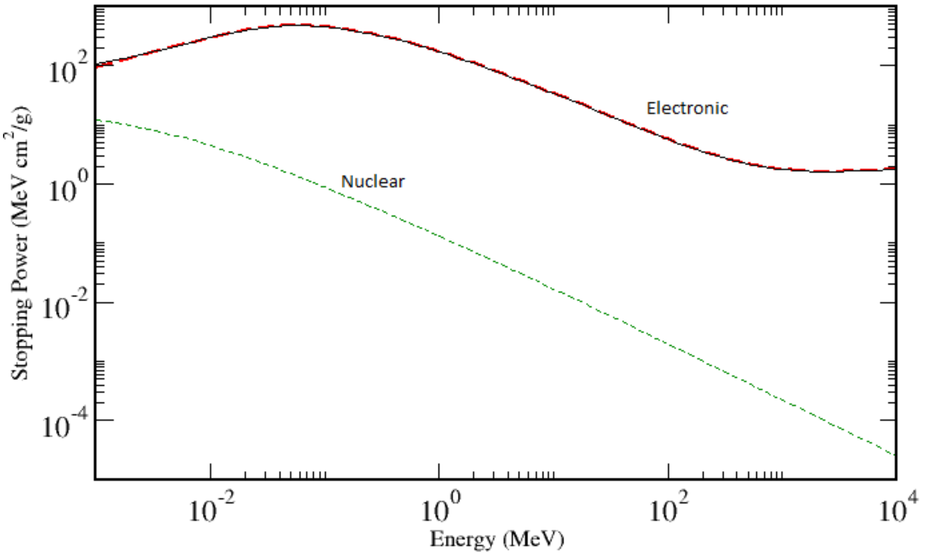

Figure 3: Nuclear and electronic stopping power for protons in aluminium versus particle energy per nucleon. From [2]

Energy loss by interaction with electrons

The incident particle or ion will transfer energy to the electrons in the solid when traveling through it. These electrons can be either excited to higher energy levels or gain enough energy to escape from the solid. As this happens, the incident particle will lose energy, most frequently the energy losses are small and this is usually described by the mean differential energy loss dE/dx (or by the stopping power S=-dE/dx). For a given incident particle and target, this energy loss has been found to be very dependent with the velocity of the incident particle. Unfortunately there is no single theorem that can describe the energy loss at all range of energy. Depending on the energy range of the incident particle, some properties from the particle and the target become relevant. The energy loss of a muon in copper is illustrated in Fig. 4. The pattern is rather complicated but allows defining three major energy ranges [3]:

Energy **[MeV/amu]**	**Gamma factor** γ	**Normalised momentum** $\beta\gamma$	**Framework**
<10	<1.01	<0.15	Lindhard
$10 - 10^6$	1.01 - 1000	0.15 - 1000	Bethe - Bloch
$>10^6$	>1000	>1000	Radiative Losses

Table 1: Energy range of the incident particle and its corresponding framework

In the mid-energy range the electrostatic stopping power is well defined by the Bethe-Bloch theory, which treats the exchange of energy between the incident particle and the atoms as the scattering of a charged particle from an isolated atom. At lower energies the velocity of the incident particle becomes comparable or even lower than the target electrons' and it is required to take into account interactions between atoms as it is done with Lindhard theory. In ultra-relativistic energy range, radiative processes such as bremsstrahlung become the dominant contribution to the energy loss.

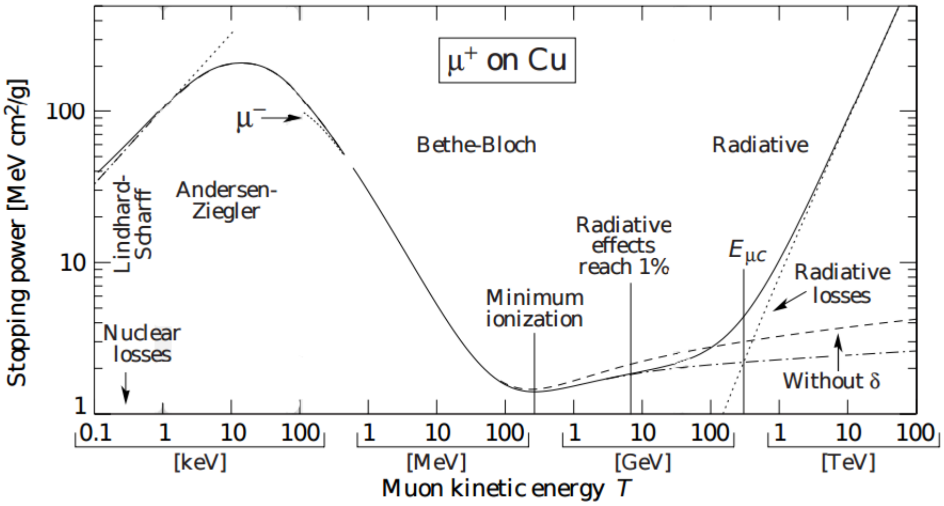

Figure 4: Electronic stopping power for positive muons on copper as function of the particle kinetic energy. The solid curve represents the total stopping power From [4]

The Bethe-Bloch theory and Range

The Bethe-Boch theory describes the mean rate of energy loss (stopping power of the material) for energies of the incident particle from $10 - 10^6 MeV/amu$ and can be described as [5]:

$$-\frac{dE}{dx} = Kz^2 \frac{Z}{A} \frac{1}{\beta^2} \left[\frac{1}{2} ln \frac{2m_e c^2 \beta^2 \gamma^2 T_{max}}{I^2} - \beta^2 - \frac{\delta\left(\beta\gamma\right)}{2} \right] \tag{1}$$

Where Z and A are the atomic and mass number of the material. Z_e is the charge of the particle, K/A is 0.307 $MeV g^{-1} cm^2$ and the $\delta(\beta\gamma)$ is a predetermined density correction necessary for high energetic particles, units are $MeV cm^2 g^{-1}$. I is the mean excitation energy for the given material, and varies from a few eV for materials with low Z to hundreds of eV for materials with high Z and can be calculated with the empirical formula:

$$I = 16Z^{0.9} \tag{2}$$

T_{max} represents the maximum energy that can be transferred to a particle in an elastic collision. It can be calculated as:

$$T_{max} = \frac{2m_e c^2 \beta^2 \gamma^2}{1 + \frac{\gamma m_e c^2}{Mc^2} + \left(\frac{m_e c^2}{Mc^2}\right)^2} \tag{3}$$

Where γ and β are the relativistic parameters, M is the mass of the projectile and m_e is the electron mass.

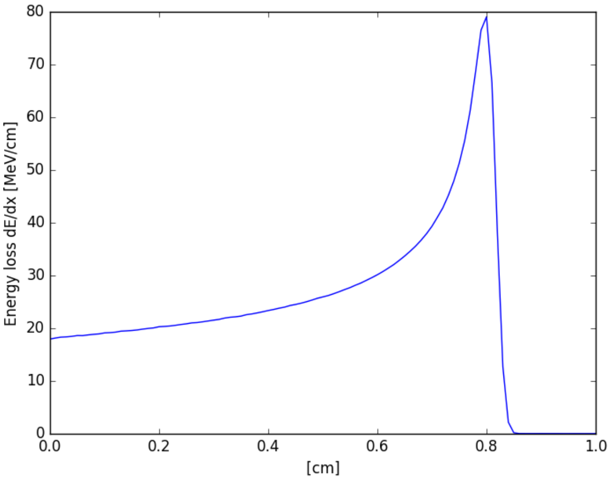

Figure 5: Bragg peak of 100 MeV protons in Tungsten. Energy deposition increases with distance, reaching a maximum at around 0.8 cm.

The energy deposition is not constant, it has a peak because interaction cross section increases as the charged particle energy decreases. In Fig. 5, we can see an example of the Bragg curve that plots the energy loss of ionizing radiation during is travel through matter. If we can just take into account the particle loses because of ionization and atomic excitation we can define the range as the distance traveled by particles in matter until their energy is (almost) zero. The range depends on the type of particle, on its initial energy and on the material it goes through. For heavy particles it can be calculated integrating the Bethe-Bloch formula [6]. After integration, the relation between the range and energy for particles above few Mev is:

$$R(E) \propto E^2 \tag{4}$$

Therefore, the range will be greater as the energy of the particle increases. For electrons, the effect of multiple scattering induces chaotic trajectories and the range is very difficult to estimate. An excellent review of all electron range-energy was recollected by Katz and Penfold who proposed the following empirical relationship for energies from 0.01 MeV to 3 MeV [6] :

$$R(E) = 412 \frac{13}{27} \frac{A}{Z} E^n \tag{5}$$

With $n = 1.265 - 0.0954 ln(E)$, E the energy of the electron, A and Z, respectively the number of nucleons and the atomic number of the material. R is given in $mgcm^2$.

Secondary Electron Theory

When a particle passes through the interface of a material, it will transfer energy to the electrons in the medium. Depending on the energy these electrons get, they can be excited to a higher energy level or gain enough energy to be emitted from the material, this emission process is known as Secondary Electron Emission (SEE). This is a surface effect so we can find this effect when the particle either enters or exits the material. Usually the electrons in the outer shells are the ones to be ionized but ionization of the inner shell is also possible although less probable. The SEE process can be provided in three steps [7]:

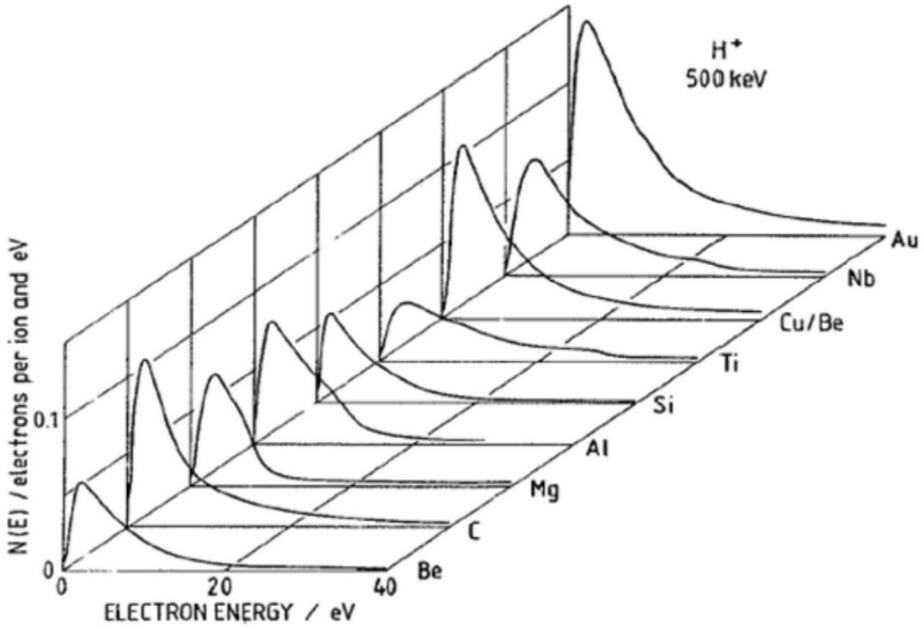

Figure 6: Ion induced secondary electron spectra for a variety of materials. In this case incident ions are protons at 500 keV. The integral of each curve in energy gives the total secondary electron yield. From [8]

The first step is the creation of the secondary electron in the bulk of the material. The minimum energy you need for creating a SE is the one required to excite the electrons above the Fermi level to the conduction band. If the projectile is an ion containing electrons these electrons can be stripped off and also produce further ionization, but if the electrons from the ion are scattered off the material, they cannot be counted as secondary electrons. The second step in the SEE process could be the diffusion in the material. When the secondary electrons travel through the material, they lose their energy. The greater the energy lose the smaller the distance they will travel.

Finally, the last step would be the emission process. In order to be emitted the secondary electrons have to have enough energy to overcome the surface potential, which is characterized with the work function $e\phi$, so the barrier height would be $W = E_F + \phi e$, with Ef the fermi level and ϕ the surface potential. The emission process is a directive phenomenon, as a consequence apart from having enough energy the electrons must have a velocity vector laying inside a escape cone with a maximum angle θ_{max} normal to the surface:

$$\theta_{max} = arcos\left(\sqrt{\frac{W}{E_i}}\right) \qquad E_i \geq W \tag{6}$$

The theoretical treatment of the SEE was formulated in 1957 by E.J. Sternglass. The main parameter describing these phenomena is the Secondary Electron Yield (SEY) which gives an average number of electrons emitted per incident particle. It can be described by the following numerical relation [7]:

$$SEY = 0.01 L_s \frac{dE}{dx}\mid_{el} \left[1 + \frac{1}{1 + (5.4 \times 10^{-6} E/A_p)}\right] \tag{7}$$

$$L_s = \left(3.68 \times 10^{-17} N Z^{1/3}\right)^{-1} \qquad [cm] \tag{8}$$

N is the number of atoms per unit volume, Z is the atomic mass of the material's atom while E and A_p are the kinetic energy and the mass of the projectile. Notice that the electronic energy loss, dE/dx, should be in $[eV/cm]$ and the projectiles kinetic energy in eV.

In Fig. 6, we can find the energy distribution of the secondary electrons emitted from different targets. $N(E)$ is related to the total secondary electron yield through $\int N(E)\, dE = \gamma$, where γ is the total secondary electron yield. As a general trend, we can see that the secondary electrons generated have an energy much smaller than the ion that has produced them. Although the exact values of these spectra are dependent on the projectile-target combination, in general it is found a sharp increase at low energies followed by a maximum at several eV and a decrease towards higher energies. Simulations of this low energy electrons are more complicated due to the limiting low energy barrier of some simulation programs such as FLUKA [9].

There is considerable experimental information available for the yield of secondary electrons ejected following the impact of a variety of ions on different solid surfaces [10] [11]. In Table 2 some results calculated using formula 8 are presented. Materials, ions and energies used in these calculations have been chosen due to their relevance for the present work. Appreciable yield differences have been reported for impact of different initial projectiles and targets, with a negative tendency with the energy of the incident ion.

Protons Energy [GeV]	**Graphite**	**Tungsten**	**Gold**	**Titanium**	**Alumina**
0.06	0.0287	0.1042	0.1073	0.0578	0.1694
0.16	0.0138	0.0534	0.0550	0.0285	0.0827
1.4	0.0054	0.0229	0.0237	0.0117	0.0334
2.6	0.0058	0.0281	0.0294	0.0134	0.0368
450	0.0047	0.0146	0.0169	0.0036	0.0091

Table 2: Secondary emision yield for protons in different materials. Calculated using PSTAR electronic stopping power and formulas 7, 8

SEY Dependence with angle of incidence

As we mentioned before the emission process in the secondary electron generation is limited with the potential barrier and the need of lying inside the escape cone. We can call L_s to the thickness of the material from which the low energy electrons can escape. If the projectile has an angle of incidence θ with respect to a perpendicular incidence to the surface, the length of the particle track increases by a factor $1/cos\left(\theta\right)$. So if we just take this into account the resulting SEY would be:

$$SEY\left(\theta\right) = SEY\left(\theta\right) cos\left(\theta\right)^{-1} \tag{9}$$

Being $SEY\left(0\right)$ the secondary emission yield for a perpendicular incidence. This formula would be quite difficult to implement because the resulting value for grazing angles tends to infinite. Experimental data has shown that for angles bigger than 70 deg the cosine dependence is no longer valid. Deviations are also encountered for heavier ions giving an angular dependence that can be parametrized as [12]:

$$SEY\left(\theta\right) = SEY\left(\theta\right) cos\left(\theta\right)^{-f} \tag{10}$$

Equation 10 is purely empirical and for angles close to 90 deg data deviate even from this behavior. Realize that the bigger the angle of incidence the bigger L_s becomes, therefore the mean value dE/dx cannot be considered constant. At the same time, the longer the distance the particle goes through, the bigger the deviation from a straight line due to multiple coulomb scattering.

Delta Rays

Most frequently the electrons generated by secondary emission have small energy, but if the energy transferred to the electron is above few hundred eV (up to T_{max}) they may be able to generate secondary ionization. This high energy electrons are called delta-rays. The number of delta rays generated by an incident ion which speed is $\beta = v/c$ in 1 cm, inside a medium of electronic density N, can be calculated with the following formula [13]:

$$n\left(T\right) = \frac{2\pi N e^4 Z^2}{m_e c^2 \beta^2}\left(\frac{1}{T} - \frac{1}{T_{max}}\right) \tag{11}$$

With Z corresponding to the effective charge of the incident ion, e is the charge of the electron and m_e its mass. T corresponds to the energy of the incident particle whereas T_{max} is the maximum possible kinetic energy transferred to an electron, that is formula 3. In order to calculate the total number of delta rays, formula 11 can be integrated from some arbitrarily lower energy limit to the maximum energy delta rays can get. Our main concern in this paper is the effect of delta rays in the generation of extra secondary electron emission. In order to have an idea of how relevant is this effect, some simulations where done. In Table 3 we present as an example the case of a 160 MeV proton beam. In order to calculate the number of delta rays we had to consider a minimum threshold energy, in this case we've considered as delta rays all the secondary electrons with an energy bigger than 100eV.

Energy 160 [MeV]	delta ray per incident proton	Total SE per pulse due to proton	Total SE per pulse due to delta rays
Carbon	0.0098	1.37e+12	2.9e+9
Tungsten	0.0202	5.34e+12	4.03e+9

Table 3: Importance of delta rays in SE phenomena. Results calculated using FLUKA software for a 160 MeV proton beam filled with $1 \cdot 10^{14}$ *Protons.*

Backscattering

When particles enter a material its path can be deflected from the initial direction because of the interactions with the material. Usually the effect results in changing the forward direction of the incident particle by a few degrees, but occasionally the particle can be deflected through a value of around 180 resulting in it exiting the material from the same side as it entered, these phenomena is what is known as back scattering. The back scattering probability is proportional to the Z of the material and it is also higher if the incident particle mass is low. In general terms, an increase in the incident particle energy is accompanied with a decrease in the back scattering probability [14].

Considering from now on the case of 160 MeV H^- , this phenomena is relevant because back scattered particles contribute to the wire signal both as missing deposited charge and as source of secondary electrons emission. Stripped protons back scattering probability is quite low and we are going to consider its effect negligible. For detached electrons, the probability of back scattering is not negligible. The electrons energy ranges from 87 keV (kinetic energy in case of stripping and elastic scattering from 160 MeV H^-) to much lower levels if they loose energy in the material in between the stripping and their backward exit point. In Table 4 we summarized some results to give the reader an idea of the contribution of back scattered electrons on the expected SEY.

Energy 160 [MeV]	BS per incident proton	Total SE per pulse due to proton	Total SE per pulse due to BS electrons
Carbon	0.05	1.37e+12	1.17e+11
Tungsten	0.48	4.34e+12	6.29e+11

Table 4: Importance of delta rays in SE phenomena. Results calculated using FLUKA software for a 160 MeV H^- *beam, (electron's energy 87keV) filled with 1e+14* H^- *particles.*

Multiple Coulomb Scattering

When a particle beam goes through matter an emittance growth is inevitable. The change on the original particle's path can be described by the Coulomb scattering theory.This theory assumes that the incoming charged particles undergo many small deflections and the final scattering angle is equal to the sum of all the small deflections. The variance of the scattering angle can be described by formula 12, suggested by Highland in 1975 [15]:

$$\langle \theta^2 \rangle = \left(\frac{E_s}{pv}\right)^2 \frac{d}{L_{rad}} \left[1 + \delta ln\left(\frac{d}{L_{rad}}\right)\right]^2 \tag{12}$$

The value of $\delta = 0.038$ and was calculated by Lynch and Dahl in 1990 [16] with an error smaller that 11% for $10^{-3} < \frac{d}{L_{rad}} < 100$. They also provided an estimation of the quantity $E_s = 19.2MeV$. It is common to work in units of the radiation lenght, L_{rad}, defined as the mean distance over which a high energy electron looses all but $1/e$ of its energy by bremsstrahlung. It is generally measured in g/cm^2 and is rigourosly expressed as:

$$\frac{1}{L_{rad}} = 2\alpha \frac{N_A}{A} \rho Z^2 r_e^2 ln \frac{a}{R} \tag{13}$$

Where $\alpha \approx 1/137$ is the fine structure constant, d being the material thickness of a material with density ρ, atomic mass A and Z the atomic number. $r_e = e^2/\left(4\pi\epsilon_0 m_e c^2\right)$ the classical radius of the electron. a is the atomic radius and R the nuclear radius. Formula 12 was the variance through solid angles. The variance of the scattering in the transverse direction can be defined as:

$$\langle\theta_x^2\rangle = \left(\frac{13.6MeV}{pv}\right)^2 \frac{d}{L_{rad}} \left[1 + 0.038 ln\left(\frac{d}{L_{rad}}\right)\right]^2 \tag{14}$$

It has to be remarked that the logarithmic correction tends to diverge when $d/L_{rad} << 1$. The accuracy of the method therefore is arguable for small material thickness. In the same publication Lynch and Dahl also formulated an estimation of the variance that is not directly dependent on the materials' radiation length and it is what the program named GEANT uses.Where ρ, A and Z are the material density, atomic weight and charge number. Even if this program has not been mentioned in these pages, it is a large well known particle physics simulator.

$$\chi_{cc}^2 = \left(0.3961 \cdot 10^{-3}\right)^2 Z \frac{\rho}{A} \left[GeV^2 cm^{-1}\right] \tag{15}$$

$$\langle\theta^2\rangle = 6.538 \chi_{cc}^2 \frac{d}{\left(pc\beta^2\right)^2} \tag{16}$$

Chapter 3

Secondary Emission Monitors (SEM)

SEMs represent a class of diagnostics based on the monitoring of secondary emission electrons generated by the primary beam passing through the detector. Different detector designs are optimize to reconstruct the transverse beam profile (e.g. wire gids and wire scanners), the beam intensity (e.g. thin foils) or other parameters like beam halo.

At CERN, SEMs are used in various accelerators, from low energy linacs to the Super Proton Synchrotron 450 GeV extraction lines towards fixed target experiments. In this chapter we will give some details about wire grids and wire scanners and only list other detector types.

Wire Grids

A SEM grid consists of thin ribbons or wires [17], which interact with the beam. Each wire experiences secondary electron emission as described in the previous chapter and therefore a charge will be generated on the wires. Each wire is connected to an individual channel, and the signal produced by each of them is proportional to the number of particles reaching the wire. Reading the current in each wire allows us to reconstruct a transverse profile of the beam with a resolution that depends on the number of wires covering the distribution and the distance between them. The minimum wire spacing available is around 300 um.

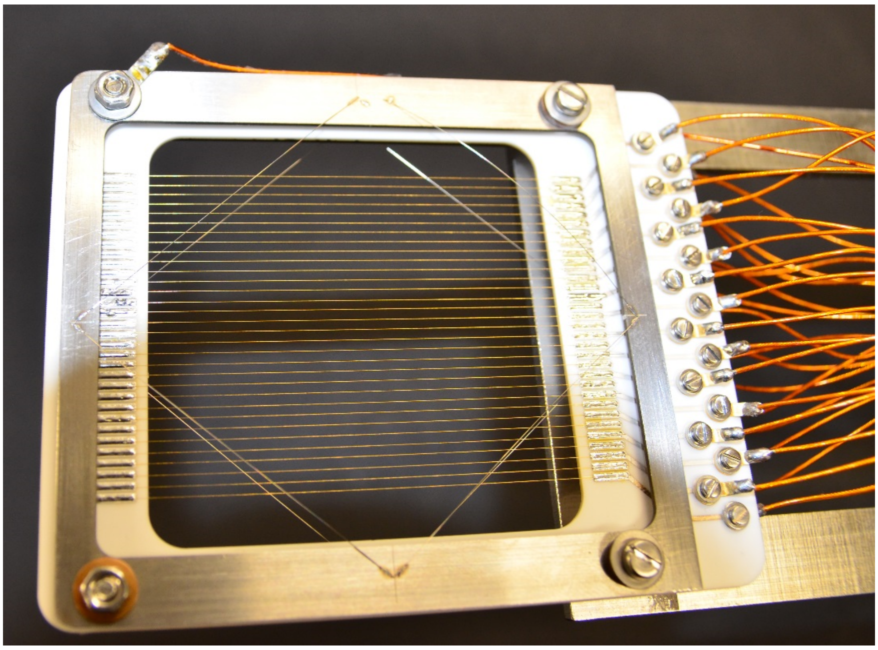

Figure 7: Example of a SEM grid installed in one of the CERN accelerators.

An example of CERN wire grid is shown in Fig. 7. The four wires at 45 degrees w.r.t. the wire grid are fixed on frames before and after the grid itself and are normally biases at few hundreds volts. When the grid is used to monitor protons, the polarity of such a voltage is positive in order to enhance the electrons secondary emission. When the grid is used to monitor negative ions (such as H^-) and the wire signal is dominated by the stripped electrons deposited charge, the voltage polarity is set to negative in order to suppress secondary emission.

SEM grids are intercepting devices, which means they can have an effect on the beam, mostly at lower energies. Therefore, they cannot be operated continuosly without affecting the beam parameters and usually they are mounted on an in/out mechanism driven by a pneumatic system. The cost of such detectors is dominated by the number of electronic channels needed, so a compromise between resolution and affordability has to be achieved.

Wire Scanners

Instead of a grid of wires, a wire scanner consists in a single wire that is moved through the beam. We are able to make a profile of the beam measuring the position of the wire and the signal induced on it at each position. Wire scanners are often two wires assembled as a cross or L-shape (see Fig. 8) and are mounted at 45^o with respect to the vertical. This allows simultaneous measurements of both transverse planes. The maximum spatial resolution is now of the order of the wire diameter $30 - 40\mu m$.

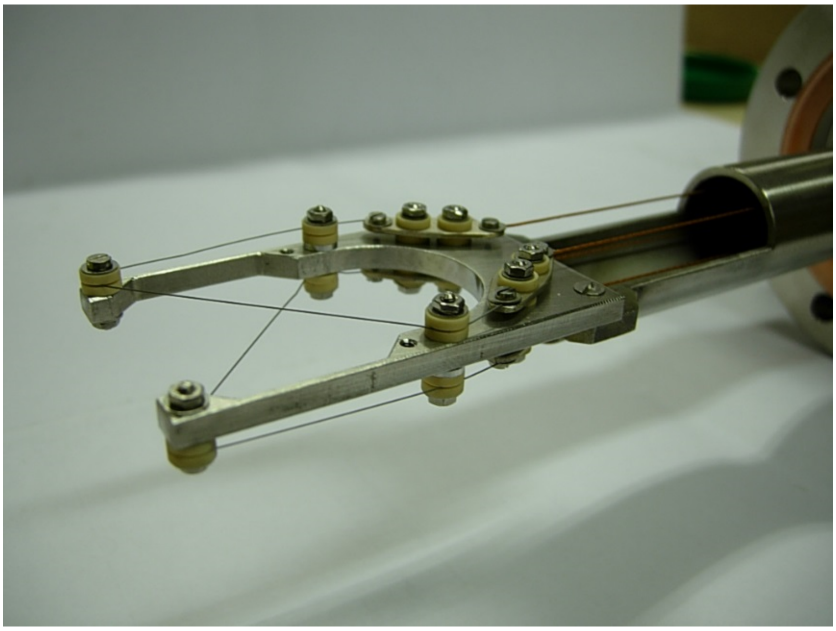

Figure 8: Example of a wire scanner used in the CERN linacs

These scanners are interesting because they only need a single electronic chain per measurement plane. They are low cost and have ultra high resolution. The problem they present is due to the time required to make a profile which can take several minutes. When used in linacs, for example, that implies that a beam scanner can only measure one profile point per linac pulse while a SEM grid can make a profile of the beam in each pulse.

Both wire grids and the type of wire scanners described here do not move during the signal recording and their use is limited to a relatively low maximum beam power, e.g. a LINAC4 pulse of 100 μs pulse length and 40 mA peak intensity. Above this limit the wires heating can end up in wire melting or sublimation. For the same reason, these devices cannot be normally used in accelerator rings where the particles circulated for multiturns consecutively. Another class of scanners, normally labeled as *Fast Wire Scanners* are used in the CERN synchrotrons (form the PSB to the LHC). They consists of fast moving mechanisms (up to 20 m/s) sweeping into the beam in few milliseconds. The beam profile amplitude signal is in this case normally extracted not by secondary emission on the wire, but from the monitoring of the secondary showers of high energy particles generated by the beam-wire interaction.

Other Secondary Emission Monitors

Apart from wire grids and scanners, other SEMs are used at CERN. In particular, the Super Proton Synchrotron (SPS), the second largest ring after the LHC, is equipped with a number of detectors dedicated to quantify and characterize the beams that are extracted to the SPS North Area facility for fixed target esxperiments:

- BSPV/BSPH or BSMV/BSMH, used to calculate the beam position
- BSPV/BSPH, which are plates split in two halves, used to measure the beam position
- BSI, which are plates used to measure the beam intensity.
- BSH or BSHS/BSVS, which are plates with a circular or rectangular hole int he middle, used to measure the beam halo.

Signal Generation in SEM.

All the phenomena discussed in the previous chapter, can be used to estimate the electric signal that is generated by a particle beam on a wire, which is part of detectors like wire grids or wire scanners, designed to sample and reconstruct the transverse beam profile. A general expression for the charge generation in the material per incident ion projectile is [18]:

$$Q\left(e/Proj\right) = -N_{elec}\cdot(1-BS)\cdot\mu + 2\cdot SEY_p\cdot\eta + 2N_{elec}\cdot SEY_e\cdot\mu + N_{elec}\cdot SEY_{BS} + Y_D \quad (17)$$

with N_{elec} number of electrons, η the proportion of incident projectiles exiting the material, μ the number of incident electrons that do not cross the material and BS the fraction of back scattered electrons. The first term quantifies the negative charge left on the material due to the incident projectile's electrons, that is the number of electrons from the projectile deposited in the material. The second and third terms correspond to the charge generated due to the SE phenomena due to the electrons and nucleus of the incident projectile. These two terms come along with a factor two because SEE is a surface phenomenon, happening at both the incident and exiting surfaces.

The third term accounts for the SE generated due to the back scattered electrons. In this case there is no factor two because only the incident surface contributes to the charge generation. Finally, Y_D is the charge created by secondary electrons generated due to delta rays. In most of the cases we have considered BS,SEY_{BS} and Y_D zero because of the smallness of these terms in comparison with the remaining ones. To give some numbers, consider the LINAC4 H^- ions as incident projectiles, for which Eq. 17 becomes:

$$Q\left(e/H^-\right) = -2\cdot\mu + 2\cdot SEY_P\cdot\eta + 4\cdot SEY_e\mu \quad (18)$$

The expected net charge generated per incident ion is showed in Table 5 for different beam energies and wire materials. The values of η and μ are material dependent and their values have been calculated using FLUKA. Considering, as an example, the case of graphite wires, the range of protons at 160 MeV is 11.6 cm and 2.5 cm at 60 MeV. It is safe to assume in this case that almost all the incident protons go through the wire ($\eta \approx 1$ in all cases).

Beam Energy [MeV]	**Electron Energy [keV]**	**Carbon (33 um)**	**Tungsten (40 um)**	**Titanium (40 um)**
60	32.69	-1.93596	-1.78510	-1.87795
100	54.49	-1.95707	-1.84995	-1.91700
120	65.38	0.03743	-1.86760	-1.92729
160	87.18	0.030411	-1.89055	0.05946

Table 5: Values of the charge [eV] generated in wires of different materials for each H^- *incident particle.*

The electrons energies are from around 30 keV to 90 keV and, in this case, the electron range in graphite varies from 11 μm up to 80 μm respectively. This implies that for 60 MeV H^- beams most of the electrons will remain in the material, generating a -2 charge, while for 160 MeV H^- ions some of the electrons will pass through the material and the charge on the wire will be only due to SEE.

As a last remark on the use of wire grids for monitoring H^- beams, it must be noted that in some cases (namely when the beam energy and the wire material/diameter are such that the impinging particles are stopped into the wire) it is useful to try suppressing secondary emission in order to have the net charge dominated by the protons and/or electrons deposited charge. Since the secondary electrons energy is normally only few eV, this can be achieved applying a relative low bias (e.g. +30V) on the wire. Another common method is to install negativly biased repeller frames before and/or after the wire detector (see Fig. 7 and related text).

It has also been experimentally proved that secondary electron suppression can be achieved using a magnetic field [19], which is re-directing the secondary electrons into the material.

Profile monitoring with SEM grids

In this section we will present the simulation of beam profile measurement with a SEM grid consisting of 40 wires 500 μm pitch and two wire types, 40 μm tungsten wire and 33 μm diameter carbon wire. We will consider an incident LINAC4 H^- beam with the parameters listed in Table 6. In the previous section, we saw the effect one H^- ion has when going through a wire. Now, instead of one particle, we consider a beam pulse populated by 10^{14} particles.

By multiplying the results found for one particle, presented in the previous section, by the number of particles that reach each wire we can re-construct the beam profile via the wire signals. Figure 9 shows the expected signal for both tungsten and carbon wires (Left 60 MeV, Right 160 MeV).

Parameter	Value	Units
Top Beam energy	160	MeV
Beam Pulse length	400	us
Repetition rate	1.2	Hz
Average pulse current	40	mA
Sigma x *	2	mm
Sigma y *	1	mm
Angular dispersion	0.49	mrad

*Table 6: Main LINAC4 beam parameters. *These two values have been selected for the purpose of this example*

For 60 MeV H^- ions we can see that the signal produced by a carbon wire, in absolute value, is bigger than the signal on the tungsten wire. In both cases the H^- electrons are deposited on the wire and SEE occurs. In the case of tungsten more secondary emission is expected and therefore the positive charge left behind due to this phenomenon is expected to be bigger than in the case of carbon.

On the other hand, for 160 MeV the signal in carbon wires is positive because most of the H^- electrons are able to exit the material. That leads to a positive signal which in absolute value is smaller than the one in the tungsten wire, which is still generated mainly by the incident H^- electrons.

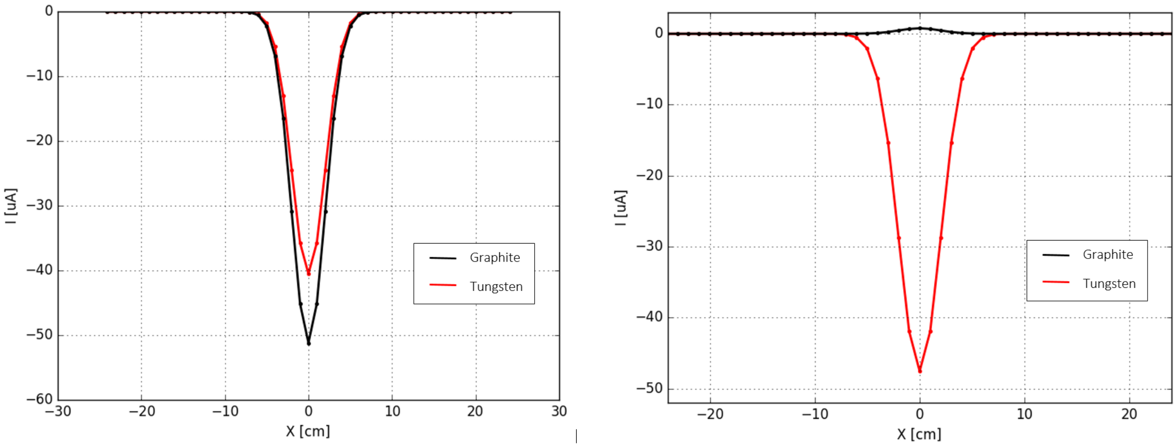

Figure 9: Expected current for Tungsten and Graphite SEM grids. Left, 60 MeV incident H^- ions. Right, 160 MeV incident H^- ions. Both cases calculated with the parameters of Table 6.

Emittance growth due to SEM

The aforementioned detectors are intercepting devices which means that have an effect on the beam. As already discussed in Chapter 2, each time a particle traverses the detector's material, it experiences Multiple Coulomb Scattering. Considering the particle ensamble, this results in an emittance increase at the monitor exit and, in case of large scattering angles, to beam losses. Such an effect is well know in literature, here we just present the result of FLUKA simulations characterizing the scattering angle.

As an example, we considered a SEM grid which consists of 11 tungsten wires of 40 μm diameter spaced 500μm, used to monitor a beam with initial $\sigma_x = 2$ mm and $\sigma_y = 1$ mm. FLUKA does not include the possibility of easily simulating H^- ions so we have studied independently the effects of the detector on electrons and protons.

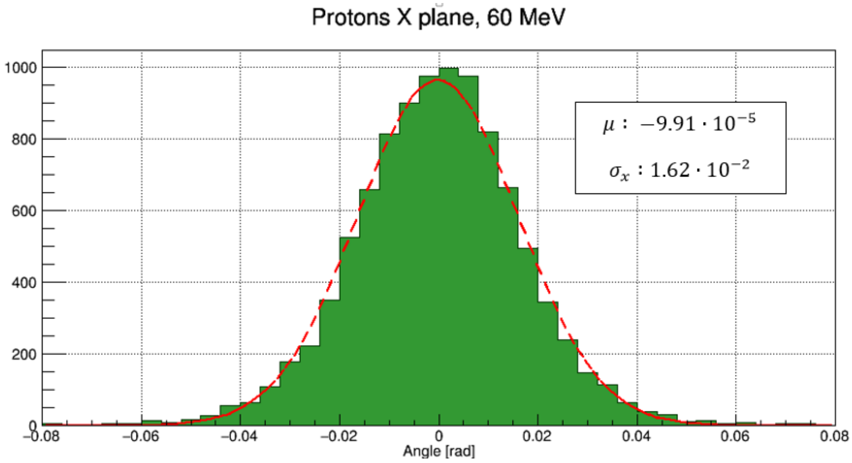

Figure 10: Histogram of protons' angular distribution with respect to the beam direction 10 cm after a SEM grid (11 tungsten wires, 40 μm thick, 500 μm pitch). Red line being the Gaussian fit of the angular distribution. For 60 MeV protons.

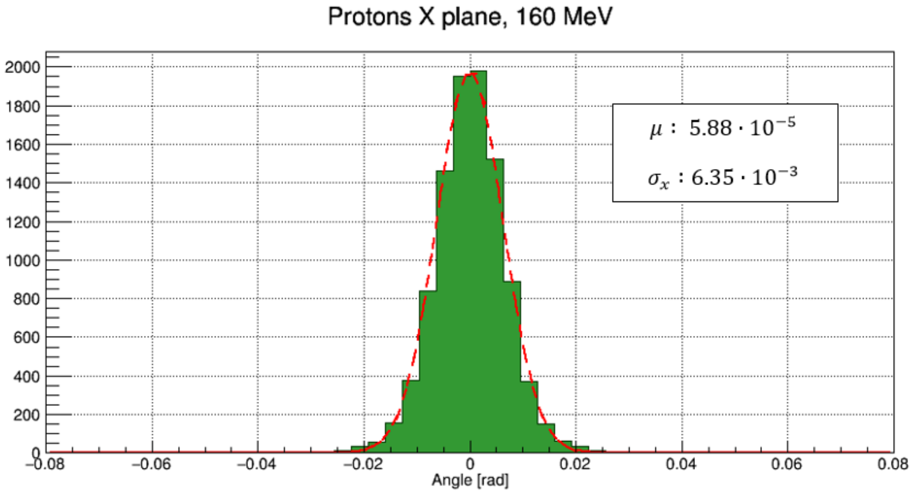

Figure 11: Histogram of protons' angular distribution with respect to the beam direction 10 cm after a SEM grid (11 tungsten wires, 40 μm thick, 500 μm pitch). Red line being the Gaussian fit of the angular distribution. For 160 MeV protons.

Figure 10 and 11 are a representation of the angular distribution with respect to the beam direction 10 cm after the SEM grid. We can clearly observe how the angular spread is bigger for 60 MeV protons (10) than for 160 MeV protons (11). This is not surprising as the probability of interactions for low energetic particles is higher than the one for high energetic particles. In this range of energies the electrons of an H^- ion would be stopped in the tungsten wires, so an study of the scattering angle is not easy in this case. If we consider more energetic ions it's observed that changes in electrons' trajectories are more drastic than changes in protons' trajectories.

Chapter 4

Study of the beam induced wire heating

During the operation of the intercepting devices as wire grids and scanners, the energy deposited by the beam into the wire material translated into a temperature increase. This can generate the loss of electrons by thermionic emission (thus affecting the wire signal) and permanently damage the wires. Accounting for the various cooling mechanisms occurring during and after the beam passage, this results in thermal cycles that are important to address in order to design the detectors and set limits for their operation.

In other words, the selection of the wire material and the the beam range of work (beam size, intensity, duration) are limited, by thermal reasons. A good understanding of the variation of the temperature and its consequences is therefore necessary [20]. The wire thermal behavior can be written as:

$$\Delta T_{Total} = \Delta T_{Heating} - \Delta T_{Radadiative} + \Delta T_{Thermoionic} + \Delta T_{Conductive} \tag{19}$$

The beam pulse causes the temperature increase in the material of the detector and it is followed by three cooling effects, radiative cooling, thermionic cooling and conduction cooling. The equations used to describe these effects are nonlinear due to the dependence of the specific heat with temperature and due to the nature thermionic cooling. As a result, in order to follow the thermal evolution, such equations have to be solved numerically.

Wire Heating

Given a beam pulse populated with N_{Tot} paritcles distributed in the horizontal and vertical coordinates according to a Gaussian shape of width $\sigma_x \sigma_y$, the temperature variations of a material sample with surface ΔS and volume ΔV can be written as:

$$\Delta T_{Heating} = \frac{N_i}{\Delta V \cdot Cp\,(T) \cdot \rho} \cdot \frac{dE}{dx} \tag{20}$$

where Cp(T) is the specific heat capacity of the material, ρ is the density, dE/dx the stopping power of the particles in the material in units of $\left[\frac{J}{m^2 g}\right]$ and

$$N_i = \Delta S \cdot \frac{N_{Tot}}{2\pi \cdot \sigma_x \cdot \sigma_y} \cdot e^{\left(-\frac{1}{2}\cdot\left(\left(\frac{x}{\sigma x}\right)^2 + \left(\frac{y}{\sigma_y}\right)^2\right)\right)} \tag{21}$$

refers to the fraction of N_{Tot} particles hitting the volume ΔV.

Radiative Cooling

In first approximation black body radiation is the dominant cooling effect and it is described by Stephan Boltzmann's law. The heat radiated from the material surface is proportional to the forth power of the temperature and it is differentiated with the black body radiation by a factor called emissivity ϵ, that in most cases depend on the temperature. Discretized to our interests the model can be represented as:

$$\Delta T_{Radiative} = \frac{\Delta S \cdot \sigma_{SB} \cdot \epsilon\left(T\right) \cdot \left(T^4 - T_0^4\right)}{Cp\left(T\right) \cdot \Delta V \cdot \rho} \cdot \Delta t \tag{22}$$

where, in addition to the variables defined above, $\epsilon\left(T\right)$ is the emissivity, and σ_{SB} Stefan-Boltzmann's constant ($5.6704 \cdot 10^{-8}\left[J/sm^2K^4\right]$).

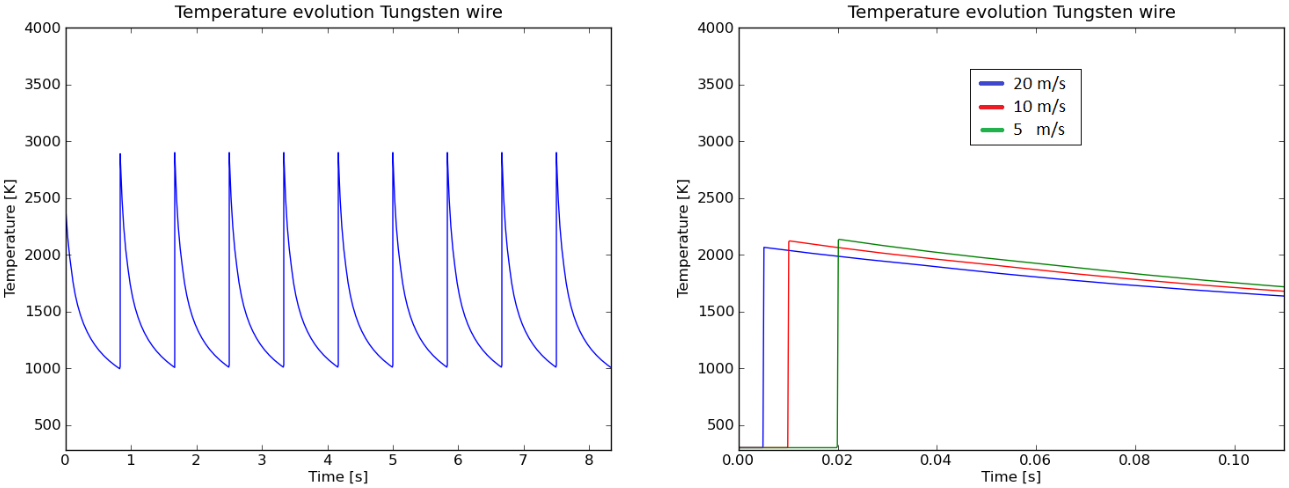

Figure 12: Left, maximum temperature evolution on a carbon wire for a SEM grid. Right, maximum temperature evolution on a Tungsten wire for a wire scanner at three different velocities. All cases for a 3 MeV, 40 mA, 100 us pulse.

Thermoionic Cooling

With the increase of temperature, thermal energy is transferred to the electrons of the material. When the energy transferred to the charge carriers overcomes the work function they escape the material, leaving a charge equal in magnitude and opposite in sign. The current density emitted by the material is described by Richardson-Dushman [21]:

$$J_{th} = A \cdot T^2 \cdot e^{-\frac{\phi(T)}{KT}} \tag{23}$$

where ϕ is the binding potential (or work function) and A is Richardson's constant, theoretically equal to:

$$A = \frac{4\pi m_e k^2 q_e}{h^3} \approx 1.20173 \quad \left[\frac{A}{m^2K^2}\right] \tag{24}$$

with m_e the electron mass, k Boltzmann's constant, q_e the electron charge and h Plank's constant. This effect, called Thermionic emission, thus generates a net positive charge that adds to SEE. In order to see how this effect can affect our SEE measurements, the thermionic current for different materials and temperatures was calculated as shown in Table 7). In most of the cases the estimated maximum temperature is below 1500 K and thermionic emission

Temperature	**Carbon**	**Tungsten**	**Titanium**	**Alumina**
300	0	0	0	0
1000	0	0	0	2.24e-14
1700	1.99e-9	1.59e-9	4.21e-9	4.64e-8
2600	1.94e-4	1.54e-4	2.73e-4	4.02e-3
3100	7.02e-3	5.62e-3	8.76e-3	1.38e-2
3500	6.14e-2	4.91e-2	7.11e-2	1.08e-1
4000	5.17e-1	4.14e-1	5.59e-1	8.31e-1

Table 7: Current due to Thermoionic emission in several materials. The numbers in red correspond to cases where the material is already melted. Melting points being 3773 K, 3695 K, 1941 K and 2345 K for Carbon, Tungsten, Titanium and Alumina respectively.

can be neglected. Above this temperature the current density increases quickly but the current due to secondary emission is still several orders of magnitude higher (for Tungsten with a LINAC4 beam it was around 1 mA). For temperatures of the order of 2500-3000 K the thermionic emission and SEE magnitudes become comparable. Since these temperature levels are dangerously close to the material melting point, both Tungsten and Carbon wires are not suitable for such high beam powers and thermionic emission will not be considered in the signal calculations discussed later.

On the other hand, we will consider the material cooling due to the thermionic emission, which can be expressed as:

$$\Delta T_{Thermionic} = \Delta S \cdot (\phi + 2\sigma_B T) \cdot \frac{J_{th}}{Cp\,(T) \cdot \Delta V \cdot \rho} \cdot \Delta t \tag{25}$$

Thermal Conduction

Due to microscopic collisions of particles and movement of electrons within a body, heat flows from hotter to colder parts of the material. In our case the part of the material that is heated by the beam core reaches a higher temperature than the rest of the material and therefore thermal conduction helps reducing the temperature in the hottest spots by transferring the heat to the colder ones. This phenomenon can be described by the Fourier formulation detailed in [20]. Nevertheless, the contribution of conduction in the cooling effects is very small compared with the radiative cooling. Because of this small contribution and the considerable increase on the simulation time, all the examples presented in this document do not consider conduction effects as a cooling effect.

Temperature simulations

To estimate the heating and cooling of the detectors we assumed that the energy deposition is constant in the direction of the beam propagation. This approximation is not accurate for cases in which the Bragg peak occurs within the material thickness, because of low particle energy and/or particular dense (or thick) materials. On the other end, the approximation holds for the cases considered below.

Table 8 shows the maximum temperatures reached in SEM grid detectors due to several incident beam types. The results show that materials with higher density are not well suited for some beam characteristics. Gold has a relatively low melting point (1437 K), which is reached in the first two cases. The rest of the materials do not reach their melting point temperature but Titanium and Tungsten are close to it in the second case. Even though Graphite has a lower SEY compared with the rest of the materials, its thermal properties make it one of the most common materials for this type of detectors. As we can see in Fig. 12 right and Fig. 13, the equilibrium is reached after few pulses. Obviously, this kind of calculations are of primary importance at the moment of designing and specifying the functional specifications of a wire detector, which must feature an equilibrium temperature safely lower than any damage threshold.

Protons 60 MeV, I = 40 mA, Pulse length = 400 μs

Material	T_{max}	Bragg peak depth $[cm]$	Energy Deposition $[MeV cm^2/g]$	Density $[g cm^{-3}]$
Graphite	755	2.03	9.642	1.7
Titanium	956	0.94	7.510	5.506
Gold	2051	0.35	5.185	19.30
Tungsten	2155	0.35	5.275	19.35

Protons 60 MeV, I = 65 mA, Pulse length = 600 μs

Material	T_{max}	Bragg peak depth $[cm]$	Energy Deposition $[MeV cm^2/g]$	Density $[g cm^{-3}]$
Graphite	1070	2.03	9.642	1.7
Titanium	1652	0.94	7.510	5.506
Gold	3943	0.35	5.185	19.30
Tungsten	3374	0.35	5.275	19.35

Protons 160 MeV, I = 40 mA, Pulse length = 400 μs

Material	T_{max}	Bragg peak depth $[cm]$	Energy Deposition $[MeV cm^2/g]$	Density $[g cm^{-3}]$
Graphite	598	11.6	4.655	1.7
Titanium	689	5.58	3.705	5.506
Gold	1379	1.85	2.657	19.30
Tungsten	1567	1.85	2.706	19.35

Table 8: Maximum temperature reached by SEM grids of different materials and for different beam types. Energy deposition and Bragg peak depth calculated using PSTAR

Even though we only discussed thermal issues, there are other processes that can lead to a wire damage, such as brittle failure, plastic failure or thermal fatigue. More details can be found in [22].

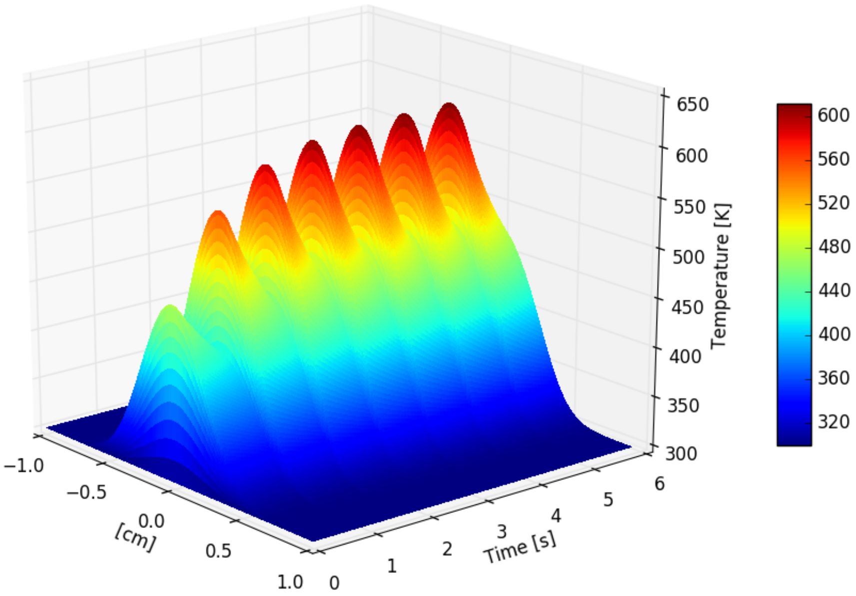

Figure 13: Temperature evolution of a tungsten wire due to 160 MeV proton beam, 100 µs

Chapter 5

Transverse beam emittance and slit-grid system measurement

This chapter contains a short introduction to the motion of particles in an accelerator and the concept of emittance. Then, it will present the slit and grid emittance measurement technique, focusing on the system used for the LINAC4 LEBT emittance characterization. The chapter ends with the review of measurements performed during this thesis work and will give some ideas for improving the monitor accuracy.

Basics of Beam Dynamics and Phase Space

The scope of the accelerator design is to guide the beam of particles along a reference path and accelerate it into the desired energy. Charged particles are accelerated and focused by magnetic and electrical fields. The reference system used to describe the movement of the particles is represented in Fig. 14. S defines the longitudinal coordinate and is always tangent to the reference path. X and Y define the transverse plane (orthogonal to the particle trajectory). x(s) and y(s) describe the particle's deviations from the reference path at each point, being x(s) = 0 and y(s) = 0 the reference path. Locally, the reference orbit has a curvature radius $\rho(s)$.

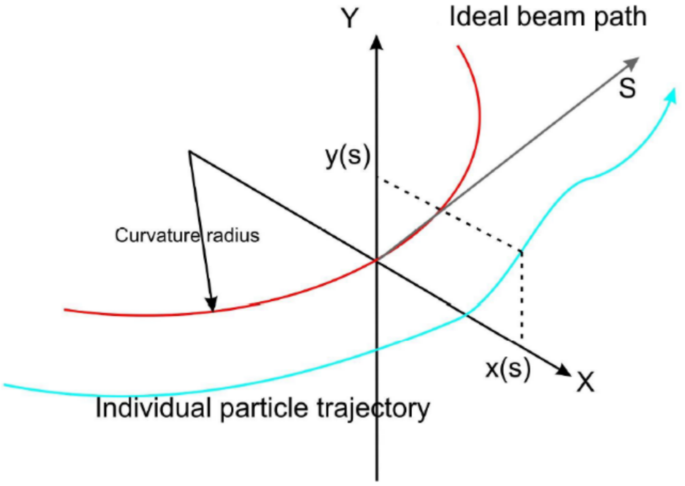

Figure 14: Coordinates system used in beam dynamics

For the purpose of this document we are going to assume that the longitudinal and transverse planes are not coupled, i.e. the motion of the horizontal plane is not affected by the one in the vertical plane and the other way round. The reference orbit is a possible particle trajectory, particles with a nominal momentum p_0 that start at some point with zero displacement will move along the designed orbit. In an accelerator facility the particle motion in the machine is usually disturbed by field errors. In addition, we do not have single particles but particles ensembles in which each particle moves in a slightly different direction but the center of gravity moves following the ideal orbit.

The principal elements of particle accelerators are those that provide the beam acceleration, guidance and focusing. The particles are accelerated by longitudinal electrical fields and the bending and focusing is provided by magnetic fields. The equation of motion of each of those particles can be derived from Lorentz's law and leads to the following expressions for the two transverse planes:

$$x'' + \left[\frac{1}{\rho\left(s\right)^{2}} + \frac{1}{\left(B\rho\right)}\frac{\partial B_{y}\left(s\right)}{\partial x}\right] x = 0 \tag{26}$$

$$y'' + \frac{1}{\left(B\rho\right)}\frac{\partial B_{y}\left(s\right)}{\partial x} y = 0 \tag{27}$$

where $B\rho$ is equal to the ratio of momentum to charge, also called magnetic rigidity. The detailed solution of those equations can be found in [23]. Each particle is going to have at each instant of time a position and momentum. The x, y space only contains spatial information of the particle distribution in a beam and merges both x(s) and y(s) in a single chart, see Fig. 15 left. Neglecting mutual interactions and coupling between the three coordinates we can define the phase space of each degree of freedom of the system (see Fig. 15 right). The phase space contains the whole description of the particles ensemble state for that particular plane.This information is required for calculating the subsequent motion of the particles in the electromagnetic fields of the accelerator.

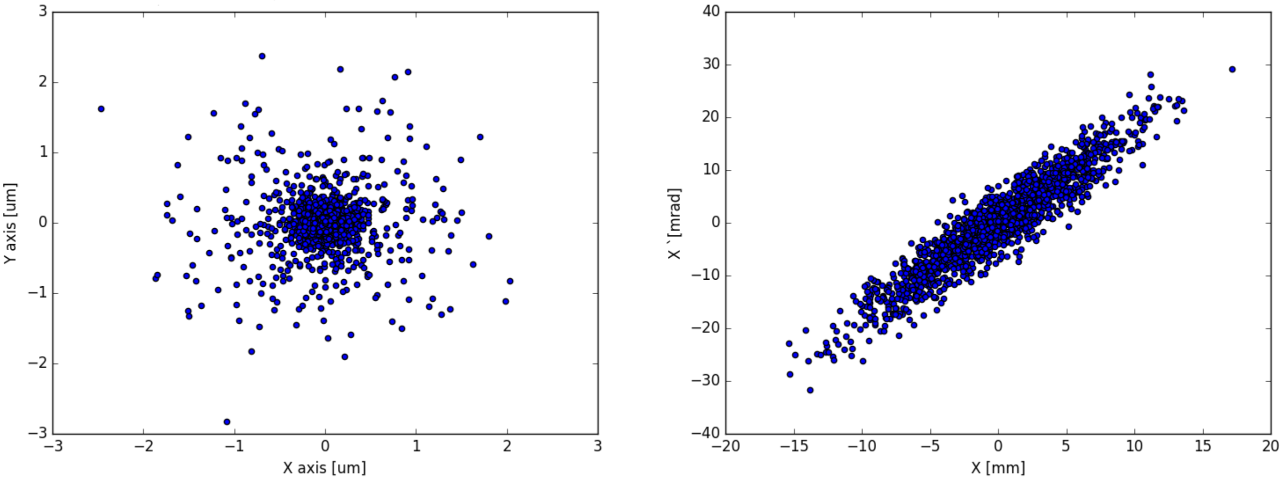

Figure 15: Left, example of x,y space. Right, example of phase space. Both images are purely illustratives

The transverse beam emittances ϵ_x, ϵ_y are usually defined as the area (optionally divided by π) of the phase space ellipse containing 95 % of all the particles. In a transfer line or in a storage ring (i.e. no acceleration) and assuming no energy losses due to radiation, even though the shape of the emittance ellipse can change, Liouville's theorem establishes that the emittance is conserved [24]. In linear or circular accelerators (i.e. for particles experiencing energy change) the emittance is not invariant but we can define the so called *normalized emmitance*:

$$\epsilon_N = \beta\gamma\epsilon \tag{28}$$

Where ϵ is quoted as geometric emittance and ϵ_N is the normalized emittance, which is conserved during acceleration.

Emittance measurement with a Slit-Grid system

For low energy linear accelerators, a typical method for measuring the transverse emittance consists in a slit-grid system, as schematically shown in Fig. 16. The system consists in a movable slit with a small aperture that moves perpendicular to the beam direction. The SEM grid is placed at a distance L. For each slit position the narrow aperture allows the passage of a beamlet populated by particles that have almost an equal position x and a certain angular distribution. Thanks to the relative intensity read in each wire we are able to know the angular distribution of the particles at each grid position (X). Therefore, by scanning he slit across the beam the whole phase-space can be reconstructed.

In order to sample both transverse planes two slits and two grids are needed. The angular resolution of the monitor is determined by the profile monitor resolution (wire separation) and the drift space between the slit and the SEM grid. The geometry and material also effects the measurement accuracy [25].

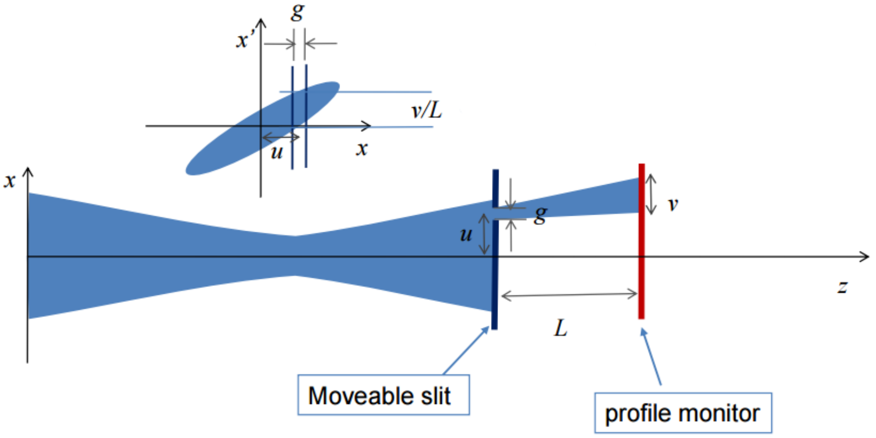

Figure 16: Schematic representation of a slit grid system

Emittance measuremets at 3MeV Test Stand

In order to obtain a stable source for LINAC4 , systematic simulations of hydrogen plasma and beam formation are ongoing. Accurate measurements of the source emittance were needed to check the reliability of these simulations and the behavior of two different geometries of the plasma chamber extraction. The following pages will discuss the emittance measurements in the 3 MeV Test Stand, the possible sources of uncertainty and propose some improvements. No further details about the source are given. If the reader is interested, more details about LINAC4 's source can be found in [26].

As mentioned in Chapter 1, between the source exit and the entrance of the first accelerator element, a Low Energy Beam Transport (LEBT) is needed to match the beam to the RFQ requirements. The LEBT is equipped with diagnostics devices to control the beam quality and to supervise the performance of the source. The following measurements were taken in the 3 MeV Test Stand which consists in a LEBT whose layout is similar to the one installed in LINAC4 . A picture of the emittance meter installed in the 3MeV test Stand is shown in Fig. 17.

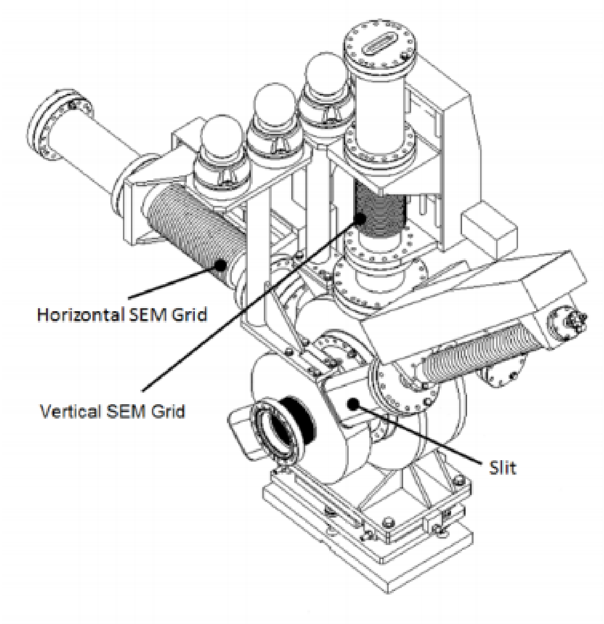

Figure 17: Scheme of 3 MeV Test Stand Emittance Meter

The system consists in two SEM grids and a stainless steel blade inclined 45 degrees relative to the vertical axis. The blade is 1 mm thick and two 100 μm gaps have been machined, one parallel to the horizontal axis and the other parallel to the vertical axis. The SEM grids are positioned 20 cm downstream the slit and consist of 40 Tungsten wires of 40 μm of diameter, separated by 0.75 mm. Both the blade and the SEM grid are moved using stepping motors and are mounted in 2 separate vacuum chambers. For each slit position, the corresponding grid can be moved with steps of 50 μm in order to improve the overall resolution.

As a first approach some measurements of the beam emittance for different initial conditions were done. In these measurements we did a fast scan, that is, for each slit position the SEM grid stayed still. In this way the measurement time was reduced considerably but the measurement angular resolution was limited. The motion of the emittance meter are limited, ±35 mm for the slit, and ±70 mm for the SEM grid, defining a spatial scan range of ±35 mm. For each slit position the electronics is digitizing the each wire signal with a sampling period of 4 μs. By scanning the slit over all 75 mm, the phase space can be reconstructed (see Fig. 18).

After this first check of the system and of the beam emittance with a coarse scan, more accurate measurements imply displacing the grid in small steps for each slit position (to overcome the wire distance limitation). In addition, one has to properly setup the control and acquisition systems (e.g. wire signal gain) and be aware of possible misinterpretation of the results. In the following we will focus on the interpretation of the various SE sources and their effect on emittance measurement accuracy.

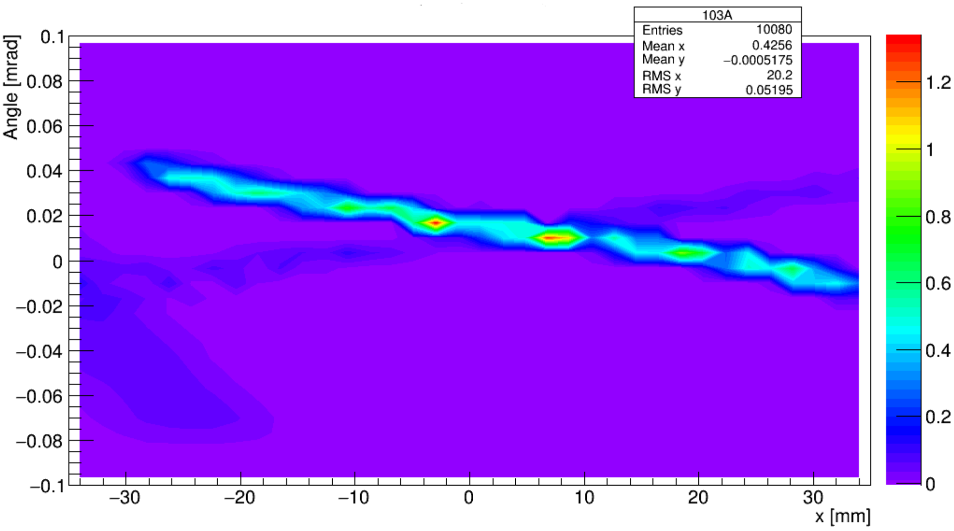

Figure 18: Emittance measurement at 3 MeV Test Stand of a proton source. Two different kinds of particles can be identified, protons and a smaller proportion of H^0

Emittance measurements accuracy

All the emittance measurements were done with 45 keV protons. At this energy, the range of protons in Tungsten is $\approx 45\ \mu m$, therefore, most of the protons reaching the $40\mu m$ Tungsten wires are stopped in them. If instead of protons the incident particles were H^- both the proton and the electrons would be stopped in the wire leaving in that case a negative charge on the wire. The output signal is thus a combination of the charge deposition and the secondary emission phenomena. The SEY in tungsten for 45 keV protons is around 1.78. According to this number even if the two electrons of an incident H^- are stopped in the wire, the signal is expected to be positive due to the strong contribution of the secondary emission.

Unlike previous cases, at this low energies we have to take into account the effect of secondary emission suppression due to negative space charge of an H^- beam. In a particle beam, we name space charge effects the interactions charged particles have within the beam pulse. The space charge force depends strongly on the particle energy and scales with $F_{SC} \approx \gamma^2$ [27]. It is also particle density dependent. Experimentally, in the energy range we are working on, it has been observed that for relatively large beam size the signal polarity is mainly positive due to the strong SEE, whereas for smaller beam sizes the signal polarity is negative due to secondary emission suppression [28]. The unwanted strong dependence of the signal polarity on the beam size motivates the study of a method to suppress secondary emission in all cases.

In order to suppress secondary emission two possibilities have been tested: biased metallic frames upstream or downstream of the grid and a bias voltage on the grid wires. The study of different scenarios was simulated using the CST Particle Studio Suite [30], a specialist tool for fast and accurate analysis of charged particle dynamics in 3D electromagnetic fields. In Fig. 19 we can find a schema of the complete geometry we have worked with. Nevertheless, for the simulations not all the elements where considered, only the relevant ones for each simulation were taken into account.

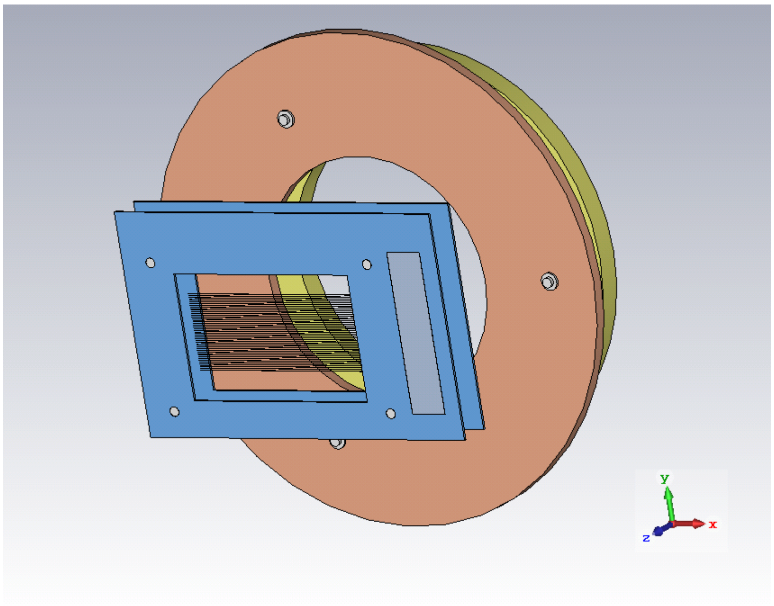

Figure 19: Scheme of the geometry used. Blue: SEM grid Orange: polarization ring 1. Yellow, polarization ring 2

Lets begin with the suppression of secondary electrons using two polarized rings. In this case we are trying to suppress the secondary emission produced on the incident and exiting faces on the wire. In order to simulate secondary electron production we considered the wires to be constant source of electrons. A typical beam size would be around 2 mm, that is $\sigma_x = \sigma_y = 2mm$. The SEM grid is made of $40\mu m$ tungsten wires with a separation of $500\mu m$ between each other. This tells us that the most affected wires are going to be the 7 central wires. Therefore, we considered this seven wires as a source of $10eV \pm 10eV$ electrons.

Secondary electrons are negative charges therefore if we bias the rings with a negative voltage, the electrons will be repelled and thus go back inside the wires. Furthermore, if the second ring is polarized with a bigger potential (in absolute value) than the first ring, an electric field between them is going to be generated, making the electrons accelerate back to the wire. This electric field can be made bigger if the first ring is biased with a positive signal (e.g. +1200 and -1200 V), but in that case the positive ring could attract some undesired negative charges. Several configurations were tested, finally the polarization Ring 1 = -600 V and Ring2 = -1200 V was selected, See Fig. 20.

The reason why we are trying to suppress SE with this two polarized rings is because they are currently installed in the LEBT. In reality these rings are placed downstream the beam direction at a distance of around 63 mm from the SEM grid and their purpose was to suppress the secondary electrons coming from a Faraday cup. Previously this Faraday cup was placed 8 cm downstream the SEM grid affecting considerably the SEM grid measurements [31]. Currently this Faraday cup is palaced $\approx 1m$ downstream the SEM grid so SE emitted from the cup are not able to reach the SEM grid and affect its measurements. At the moment these rings are no longer useful for this purpose and as they are already installed they could be used to cover other problems. Although the rings are placed downstream the SEM grid, in our simulations we've considered them to be before the SEM grid in order to suppress the secondary electrons generated on the incident surface.

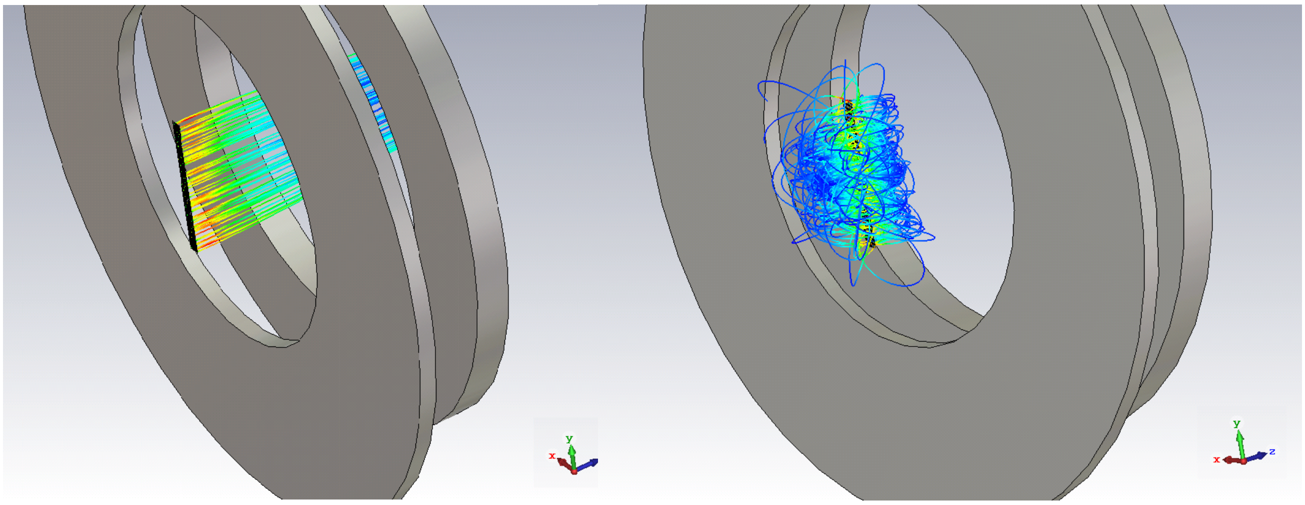

Figure 20: CST Particle Studio simulation of the effect of polarized rings on secondary emission surpression. Left, no polarization on the rings. Right, Ring 1 = -600 V, Ring 2: -1200V

Now lets go back to our second objective, that is, trying to suppress secondary electrons emitted at angles around 90 and 270 degrees with respect to the angle of the particle's incidence. These electrons are going to collaborate with the SE problem and also generate some cross talk with the neighbor wires [32]. In this case both positive and negative bias can be used to suppress SEE. If we use a positive bias in a wire we are actually increasing the work function and making it harder for secondary electrons to escape from the material. The problem with this method is that wires can also attract some undesired background electrons. The other option is to use negative bias in nonconsecutive wires. That allows us to repel background electrons and at the same time surprises secondary emission on the non polarized wire.

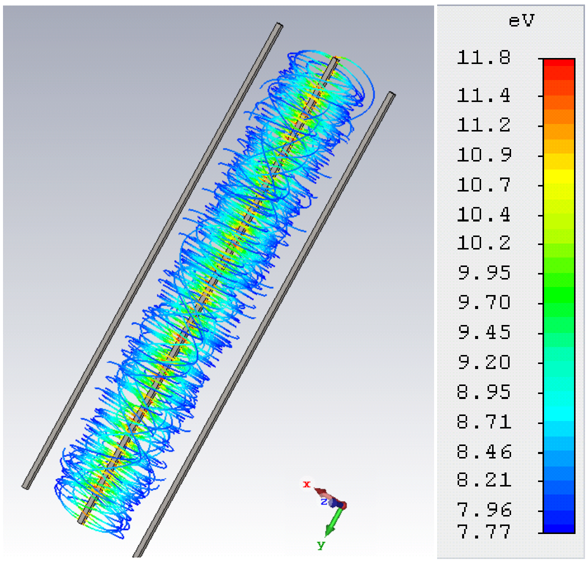

Figure 21: CST Particle Studio simulation of the effect of secondary emission supression with polarized wires. In this case the wires on the extremes are polarized at -10 V. The scale is aplicable in all the previous cases.

In Fig. 21 we can see an example of $40\mu m$ Tungsten wires with the central wire as an electron source and the neighboring wires polarized at -10 V. The main problem with this method is that negative polarized wires cannot be used afterwards as a source of information to reconstruct the beam profile, so the accuracy of the measurement is affected. It is necessary to mention that all the results aforementioned have not been experimentally tested yet, they are only simulation results. So before concluding in their possible utility, further tests are necessary.

Chapter 6

LINAC4 's $H^0 H^-$ Monitors

At the moment, Linac2 is the first in the proton acceleration chain. The protons are accelerated form the few keV source to the 50 MeV LINAC2 top energy. As already discussed above, the LINAC2 will be replaced in 2019 by the new LINAC4 , which will bring H^- particles up to 160 MeV. The injection into the PSB (4 rings, one on top of each other) will be performed by means of a H^- charge exchange injection system, through a Carbon stripping foil (one per ring), converting $\approx 99\%$ of the beam to protons. In this chapter we will talk about the charge exchange injection, what a stripping foil is and we will explain the arrangement of the H^0/H^- dump in the injection system. The core part of the chapter will focus on the new H^0/H^- monitors, their setup and the detailed explanation of their calibration procedure.

Charge exchange injection (CEI)

Among other upgrades, it is foreseen to increase the LHC luminosity by providing the collider with more bright (high density) beams form the injectors. At the moment, the first of the brightness limitations is represented by space charge effects in the PSB, which will be strongly reduced increasing the PSB injection energy from 50 MeV to 160 MeV. A further brightness improvement is expected from the charge exchange injection (CEI) [33]. The process consists in the stripping of electrons from H^- ions, followed by the capture of the new generated protons by the circular accelerator. Having the injected and circulating beam with opposite charge polarity, will allow increasing the density of particles in the beam.

The 160 MeV H^- beam from the LINAC4 needs to be distributed to the 4 superposed synchrotron rings of the PSB. After the beam is deflected to the four appropriate apertures, it will be injected into the PSB by means of an CEI system. Figure 22 shows the layout of

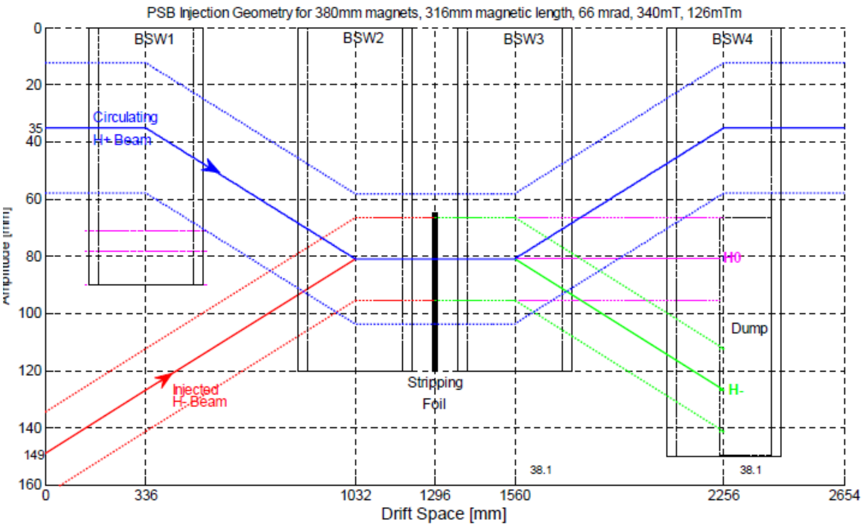

Figure 22: LINAC4 PSBooster injection Layout

the injection system. At each ring a set of 4 dipole magnets (BSW) will create the required injection bump and a stripping foil will convert the H^- beam to H^+. Four internal H^0 H^- beam dumps will be installed downstream each stripping foil in order to absorb any residual partially stripped H^0 and unstripped H^- .

As already mentioned, the fundamental adventage of this technique is that due to the opposite charge of the injected and circulating beams the CEI can be designed for injection of succesive turns into the same phase space, increasing in this way the brightness of the beam [34].

Stripping Foil

In between the two BSWs we can find a foil. This foil is in charge of stripping the electrons from the H^- ions, thus generating the protons to be injected into the PSB. Commonly, Carbon stripping foils are used. Carbon foils have the advantage of being the material with the lowest Z that can be fabricated into a very thin foil, it is stable in vacuum at high temperatures and has good electrical and thermal properties [35].

After the H^- beam goes through the stripping foil we can find three types of particles remaining, H^+ (protons), if two electrons were stripped, H^0 if only one electron was stripped and H^- if neither of the electrons were stripped. There could also remain other types of particles due to the possibility of electron pick up. However, for energies above 100 keV the cross sections for electron pick up can be neglected. The ratio of H^+ after the stripping foil is given by [36]:

$$f_{H^+} = 1 - \frac{1}{\sigma_{-1,0} + \sigma_{-1,1} - \sigma_{0,1}} \left[\sigma_{-1,0} e^{-\sigma_{0,1} x} - (\sigma_{0,1} - \sigma_{-1,1})\, e^{-(\sigma_{-1,0} + \sigma_{-1,1}) x} \right] \tag{29}$$

where $\sigma_{-10}, \sigma_{01}, \sigma_{-11}$ are the cross sections of the reactions $H^- \to H^0 + e^-$, $H^0 \to H^+ + e^-$ and $H^- \to H^+ + e^- + e^-$, respectively. $x = N_0 \tau / A$, where A is the atomic number of the Carbon foil and τ is the area density. The stripping inefficiency can be expressed as:

$$f_{H^-} = e^{-\sigma_{-1,0} x} \tag{30}$$

Therefore, the yielding of H^0 can be expressed as:

$$f_{H^0} = 1 - f_{H^+} - f_{H^-} \tag{31}$$

Table 9 shows a summary of the cross sections at different energies. For a given foil thickness the stripping efficiency is higher if the energy is lower. Also, a relation between stripped electrons and foil thickness can be found. The proportion of H^+ and therefore the proportion of stripped electrons increases as the foil thickness increases, whereas the proportion of H^0 has a maximum for a given thickness. The proportion of H^- decreases with the foil thickness.

Even if the efficiency is bigger for smaller energies and thicker foils, we have to pay attention to the temperature evolution of the foil and the effect it has on the beam emittance. In the charge exchange injection, both H^+ and H^- cross the foil and deposits energy on it. The thicker the foil and the lower the energy, the greater the energy deposition and the beam

	80 MeV	**250 MeV**
$\sigma_{-1,0}$	3.17	1.35
$\sigma_{0,1}$	1.24	0.53
$\sigma_{-1,1}$	0.056	0.024

Table 9: Cross sections of the reactions $H^- \rightarrow H^0 + e^-$, $H^0 \rightarrow H^+ + e^-$ *and* $H^- \rightarrow H^+ + e^- + e^-$. *Units* $10^{-18} cm^2$. *From [36]*

emittance blow up.

In the case of LINAC4 , several foil types are being tested. The foil will need to be about 20 mm high and 20 mm wide, with a thickness between 100 and 200 $\mu m/cm^2$. During injection, it is expected to find a current of H^0 around 2% of the LINAC4 beam pulse current corresponding to an stripping efficiency of 98%. The level of H^- coming from the stripping foil would be even lower, around 10^{-6}%, although the current of H^- can be higher because of the halo particles of the beam that miss the stripping foil.

$H^0 H^-$ Monitors in PSB HST

As discussed above, the future injection of LINAC4 's beam into the PSB will be based on the CEI technique. The PSB comprises 4 rings and one of this injection structures will be installed in each ring. The magnetic field of the BSWs is such that the protons reach the circulating beam, see Fig. 22. H^0 and H^- are not going to be affected by the magnetic field on the same way as protons. H^0 are neutral and will not be affected, whereas H^- are going to be bent in the opposite direction. These unwanted H^0/H^- particles will be stopped by a dump, see Fig. 23. H^0/H^- monitors will be installed in front of each dump in order to monitor the stripping efficiendy and so to assure a good injection. The system was tested for the first time in the PSB Half Sector Test (HST) where all the measurements explained in the following sections were taken. Other measurements results can be found in [37].

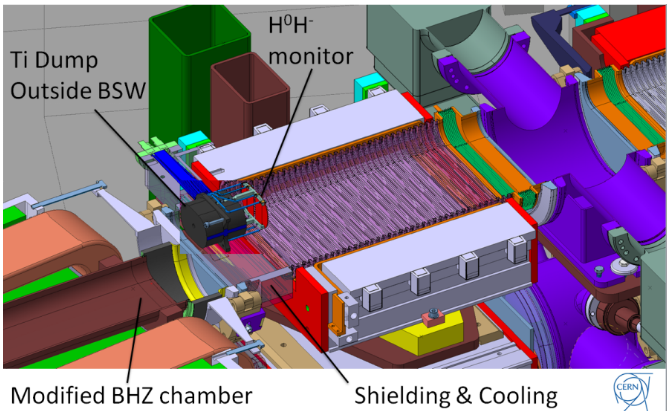

Figure 23: Mechanical representation of the H^0H^- *dump and monitors on the beam pipe.*

These H^0H^- monitors consists in two Titanium plates of 1 mm of thickness. Each plate is divided in two halves with a cut placed on the center. This additional feature adds beam position information to the intensity measurements. The monitors were placed inside the BSW4's magnetic field at a distance of 4 cm from the dump's face. This distance is enough to avoid the secondary electrons coming from the dump to affect the monitors' signal. These monitors are connected to an interlock circuit, that is, if the intensity measured surpasses a safety limit, now set to 10% of the LINAC4 's peack intensity, the interlock circuit will stop the beam. So far this feature is not yet implemented as the monitors are still being tested. Before reaching that point, the monitors and the electronics behind them have to be calibrated and cover all their required features.

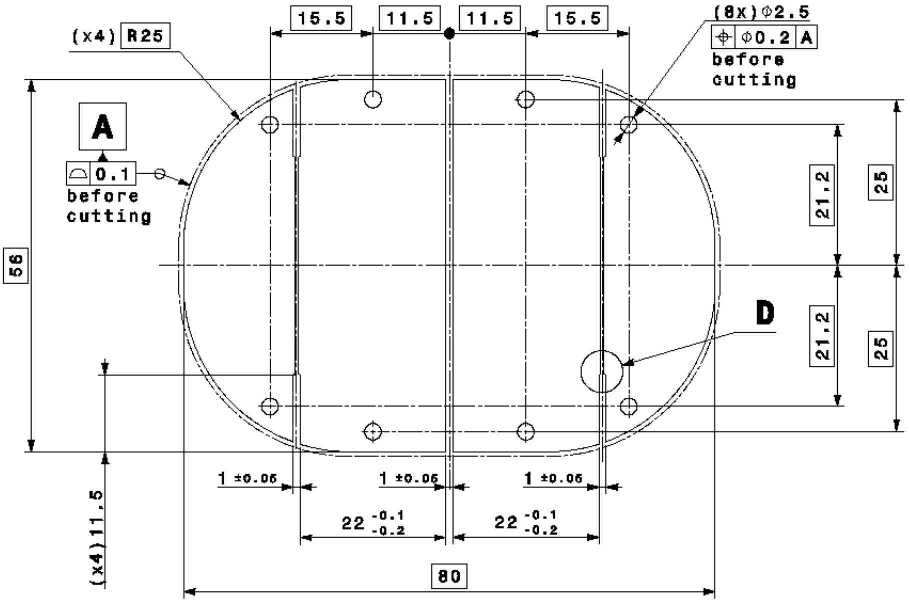

Figure 24: Production drawing of the H^0H^- plates with dimensions and tolerances.

During normal operation, the current in the H^0 plates is expected to be up to 2% of the nominal LINAC4 's current, which corresponds to around 0.5mA. Stripping degradation can be tolerated until 10% of the nominal intensity which would correspond to a signal of $\approx 4mA$. This should be the threshold at which the interlock circuit stops the beam. In a very first approximation the expected signal per impinging H^- would be 2 electron charges and 1 electron charge for H^0 plates. A more precise determination of the net charge left per incident particle can be found in Table 10.

	BS	SEY BS	δ	$H\,[e/H^-]$		$H\,[e/H^0]$	
				w S.E	w.o. SE	w SE	w.o SE
Titanium	0.23	0.0114	0.025	-1.42	-1.49	-0.61	-0.7336

Table 10: Expected net charges per impinging 160 MeV H^0 and H^- particle in 1mm Titanium plate.

The electronics readout is designed for integrating the charge in each plate between 50 ns and 1 μs. So the total number of charges read at each plate will depend on the beam intensity, beam pulse leangth and integration time. The injection time can vary between 50 ns to 150 ns. The 50 ns lower limit has been specified to be consistent with the minimum detectable signal.

Electronics conceptual design and available signals.

The electronics after the monitors are designed to ensure a continuous measurement of the H^0H^- particles, to function as an interlock system to protect the dump and therefore to assure an efficient injection. Only a conceptual explanation is going to be given in this section, for more detailed description the reader may check [18]. Several versions of the electronics where tested during the measurements but all of them shared the same basic structure.

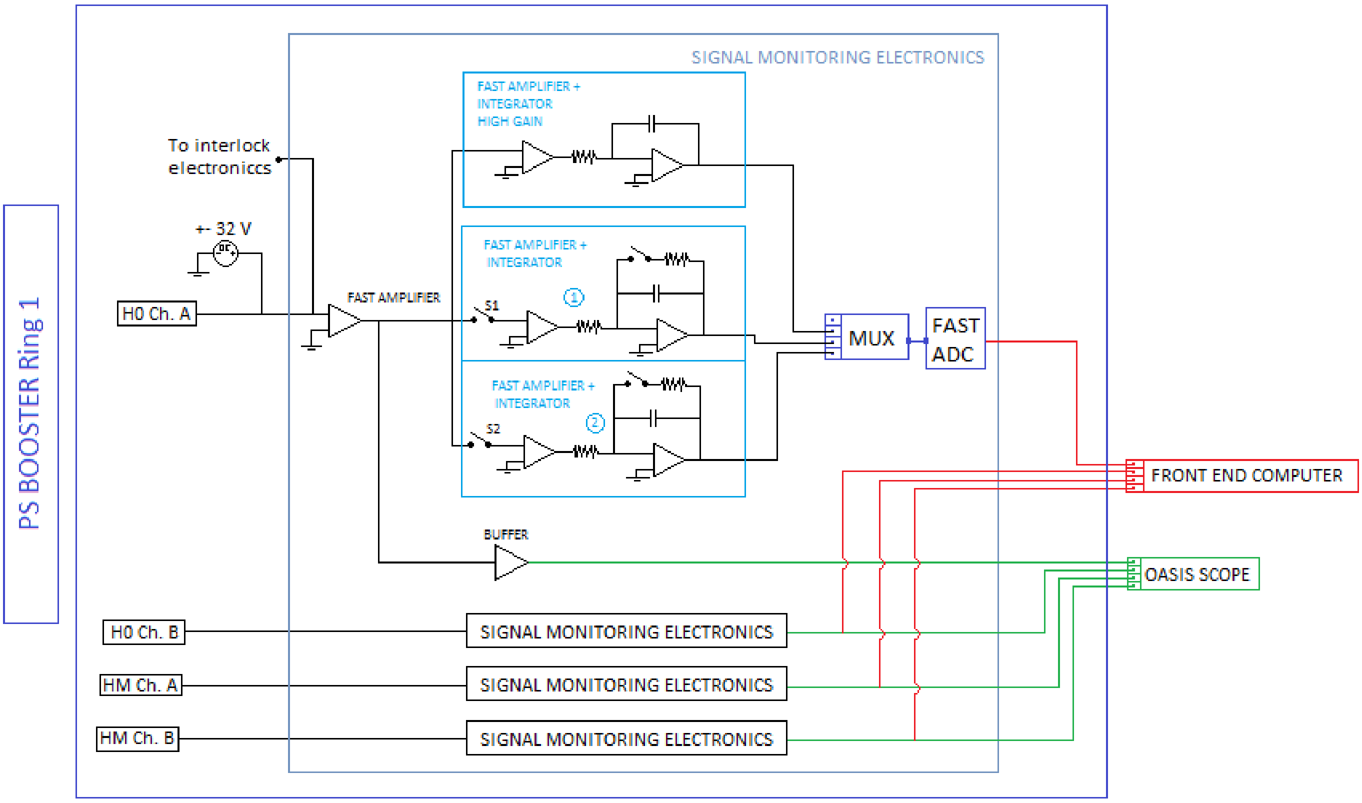

Figure 25: Schematic layout for the continuous monitoring system.

The system is divided in two main subsystems, the interlock circuit and the continuous monitoring system. One of the requirements is that the signal does not saturate even in the case of foil breakage. For this reason the continuous monitoring system has been split into two sub-circuits, high gain electronics and low gain electronics. With the high gain electronics the pulse length can go down to 50 ns but requires a long time for discharging the integrators. The low gain electronics allows the pulse to be longer than 70 ns, it includes two alternating fast integrators connected to a fast ADC that converts the integrated charge into digital samples spaced 1 μs. In this continuous monitoring circuit, shown in Fig. 25, also an unprocessed signal is at our disposal. This signal is connected to an oscilloscope channel (named OASIS) after passing through a fast amplifier. The interlock circuits on the board, see Fig. 26, comprises a slow and low gain amplifier fed with the outputs of each plate. The integrator will be connected to a comparator (or two consecutive comparators depending on the version of the circuit) that has as a second input a predefined reference.

In the following sections we are going to talk about the analysis of the signals coming from the OASIS scope, the ADC converter. Not a lot of details concerning the interlock signal will be given.

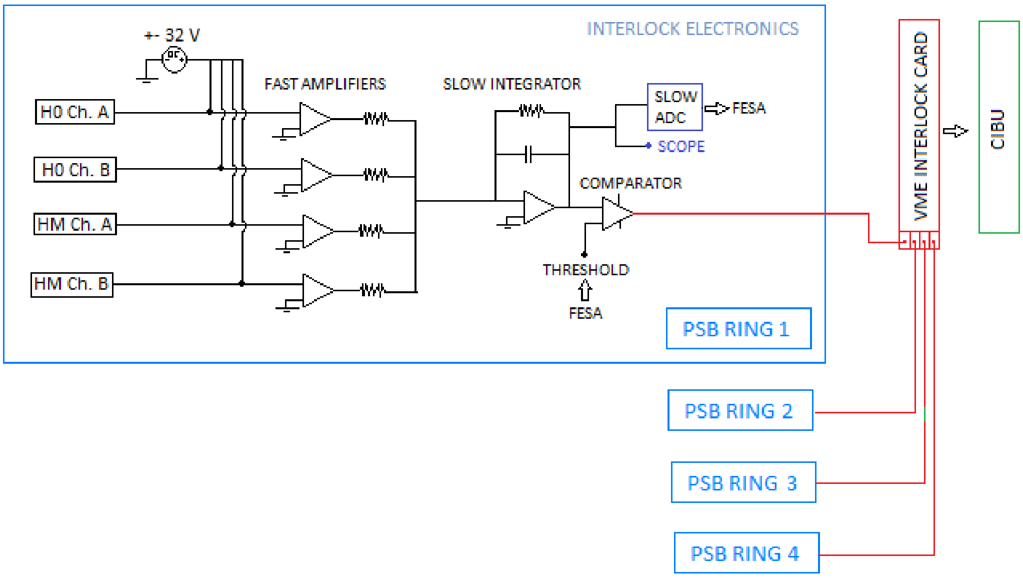

Figure 26: Schematics of the interlock circuit.

Measurements procedure.

The main goal of these measurements was to obtain a calibration factor which, independently of the intensity or type of beam, was able to relate the signal on the plates with the number of particles reaching the dump. For that, several measurements with different beam lengths and intensities were taken. The procedure of the measurements was always the same. The beam was scanned along the four plates from left to right giving special attention to the points where the beam was between two plates and when it was at the center of one plate. The sequence of the measurements was the one indicated in Fig. 27. In the following pages we will refer to those points as H0L, H0LH0R, H0R, H0RHML, HML, HMLHMR, HMR respectively.

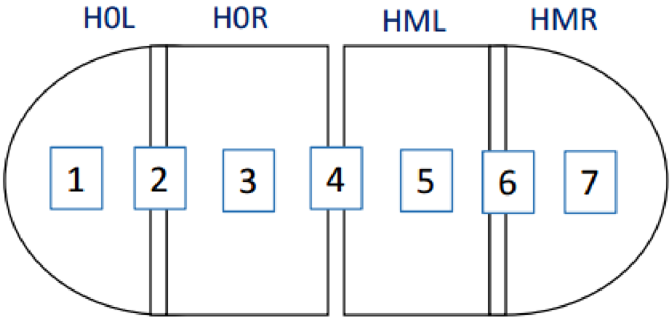

Figure 27: Schema of the order followed during the measurements.

In order to find the calibration factor the measurements were done with an H^- beam impinging directly to the plates rather than first going through the stripping foil. This approach was chosen in order to reach all the plates with a beam of the same characteristics. If the beam goes through the stripping foil, the particles reaching the monitors are going to be mostly H^0 , in a quantity dependent on the foil's efficiency. At the same time, if the incident particles were H^- it was possible to reach all the plates by choosing an appropriate magnetic field value for the BSW3 and BSW4 magnets. On the contrary, if the particles were H^0 , only the first two plates were reachable.

Oasis Signals and first conclusions

When referring to OASIS signals, we are actually referring to the analytical signals coming from the plates. Only a fast amplification is applied to these signals before going to the scope. Image 28 shows an example of the type of signal read out by the plates. Two different procedures were followed in order to analyze these signals. The first consisted in calculating the signal integral in time. This allow us to obtain the total number of charges detected by the plate in one beam pulse. Afterwards, this value was normalized by the total number of charges detected by the closest Beam Current Transformer (BCT). The second method consisted in calculating the mean value of the signal along the pulse and normalizing it by the current measured by the BCT. Both types of analysis seemed to give pretty similar results. The integral method was finally chosen for practical reasons.

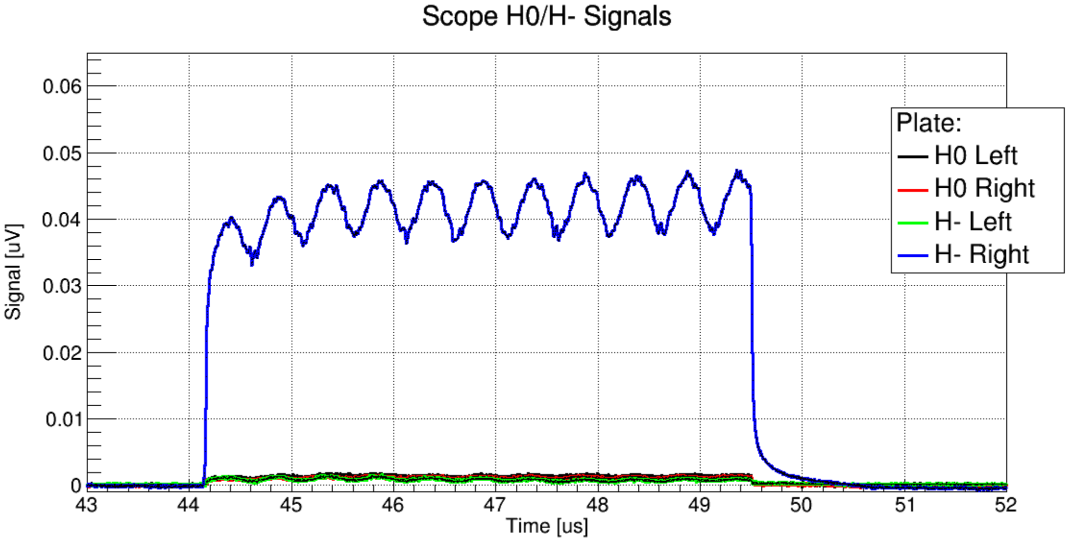

Figure 28: Example of OASIS scope traces of a 4 mA,5 μs H^- *beam. In this case the beam was placed on the center of the HMR plate.*

Figure 29 summarizes the response of the plates to different intensity beams. In this particular set of measurements, we were interested in understanding, qualitatively, how the plates responded to different beam intensities and also to see, if a different response was appreciated between the different plates. In order to appreciate this relative difference, Fig. 29 is also normalized by the value of signal measured in H0L plate. From this graph we can see the effect of the plate's gaps (1 mm). In the majority of the measurements it is also evident that the H^- plates provided a slightly higher signal than the H^0 ones.

As mentioned in Chapter 2, it has been experimentally demonstrated that secondary emission can be suppressed by using magnetic fields. In our scenario, we scan the beam along the plates thanks to BSW3 and BSW4's magnetic fields. Particularly, for the beam to reach

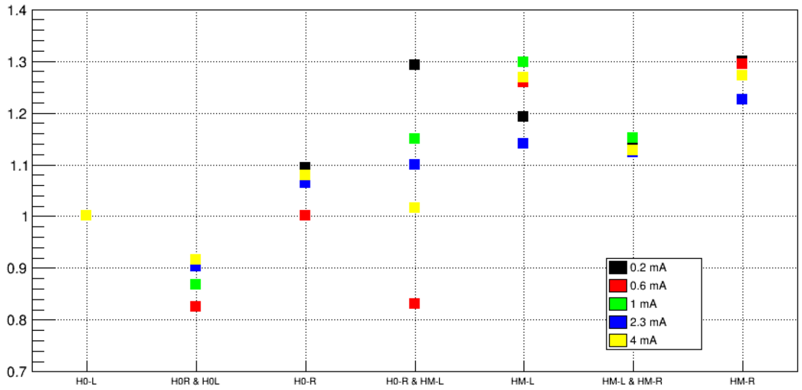

Figure 29: OASIS measurements for different beam intensities. Beam scanned using both BSW3 and BSW4. X axis, position of the beam at the moment of the data extraction. Y axis, each point represents the sum of all the signals of the plates for that particular intensity and position normalized by the number of charges measured by an upstream BCT and also divided by the signal on the H0L plate.

H0R plate, no magnetic field was needed. In order to reach H0L a very small magnetic field was necessary whereas if we wanted to reach the H^- plates it had to be higher. In the plates the signals are mostly negative due to the charge deposition of the incident H^- ions. Due to SE, electrons are emitted from the surface making the signal to become less negative. If SE is suppressed by magnetic fields it would explain why signals on the H^- plates are higher than the H^0 plates' signals. In order to check this theory, several measurements were done scanning the beam only with BSW3 and keeping BSW4 to a constant value. The monitors are placed inside BSW4's magnetic field so keeping BSW4 at a constant value of around 0.12 Tm would make SE the same for all the measurements. Figure 30 shows the summary of these measurements. In this figure it is clearly appreciated how the signal difference between the H^- and H^0 plates is no longer existent, thus confirming the SE suppression by the BSW4 field theory.

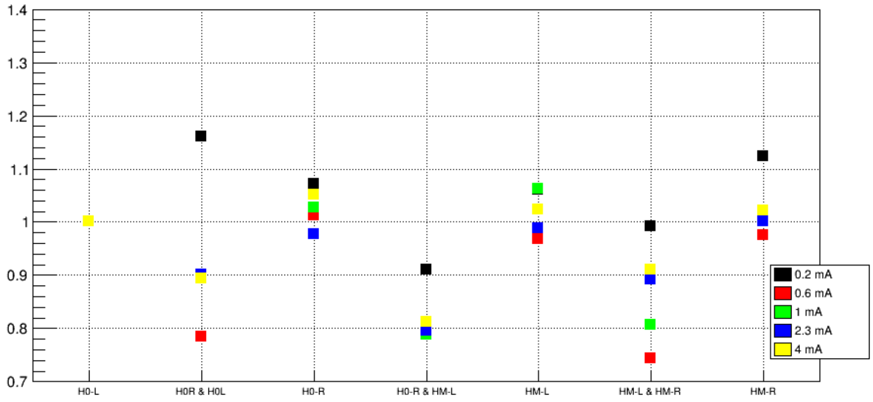

Figure 30: OASIS measurements for different beam intensities. Beam scanned with BSW4's magnetic field constant.

Digitized signals and calibration factor.

The procedure followed to analyze OASIS signals was also followed in order to analyze the signal of the plates after the electronics. The effects of the holes and the tendency up for the H^- plates was, as expected, also observed with the digitized signals. In order to study the response of all the plates under the same conditions, all the following measurements were taken with BSW4's magnetic field at a constant value. In this analysis we were interested not only in a qualitative result but also in quantifying a calibration factor able to relate the signal read out by the plates with the total number of particles reaching the dump. A linear behavior with the intensity was expected. The higher the intensity the higher the read out signal.

In Fig. 31 a summary of the digitalized signals is presented. Each point of the graph corresponds to the signal read out of the respective plate normalized by the number of charges detected by the last upstream BCT. We can clearly differentiate two different families of groups. Group 1, points around $0.6 \cdot 10^{-6}$. Group 2, points around $0.3 \cdot 10^{-6}$. Each group corresponding at each one of the versions of the electronics that were tested during the measurements. Several uncertainties were observed with the latest version of the electronics (Group 2), so espetial attention will be given to the Group number 1.

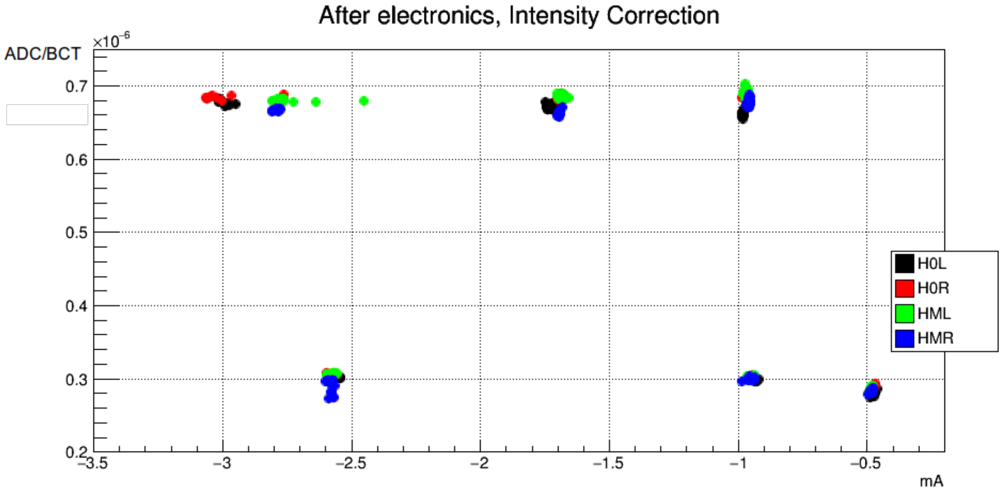

Figure 31: Signal read out by the different plates and for different intensity values. Normalized by BCT.1043's intensity . Each color corresponds to each one of the plates. Two groups of points are sighted, Group 1, points around $0.6 \cdot 10^{-6}$*, measurement done 3rd and 4th of April. Group 2, points around* $0.3 \cdot 10^{-6}$*, measurement done 6th of April. Each group corresponding on a version of the electronics behind the detectors.*

In Fig. 31, due to the normalization by the BCT's measured charges, instead of obtaining an straight line with a constant slope, the points on the graph are distributed along this slope value. A more accurate approach to this slope value is shown in Fig. 32. On the top part of the image we can find an histogram of the different registered values, the mean value being $6.807 \cdot 10^{-7}$. In Fig. 32 bottom, we can find the relative errors from the measurements with respect to this mean value. Some variations are found between plates and beam intensities, but all the values are around $6.807 \cdot 10^{-7}$ with a relative error smaller than ±2%.

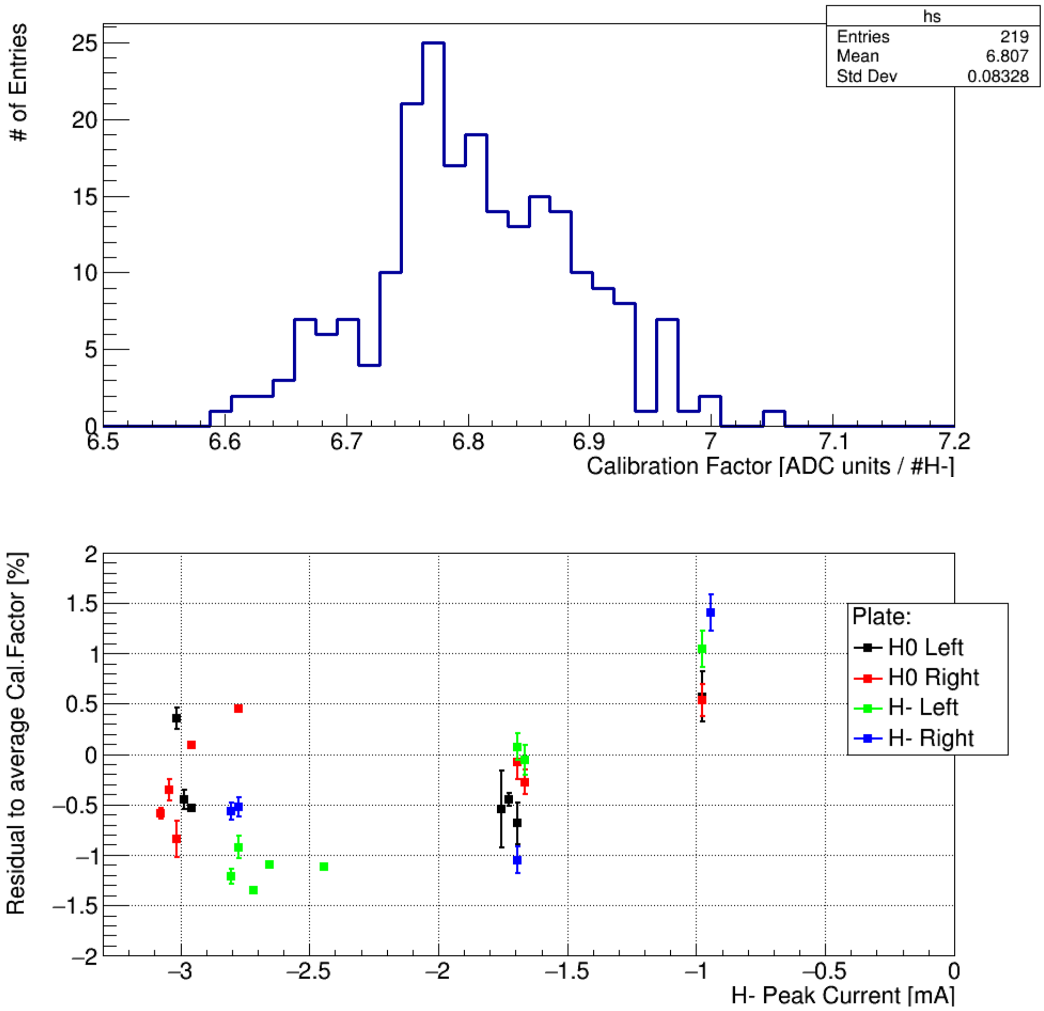

Figure 32: Top, histogram of the callibration factor (Digital signal / BCT signal) for different intensities and plates. Bottom, Relative error in % of the callibration factors for different plates and intensities. Both graphs corresponding to the version of electronics tested the 3rd and 4th of April.

Reliability of k factor for H^0 signals.

A second set of measurements was carried out while testing different stripping foils. As in the previous measurements, several beam intensities were used. Figure 33 summarizes the response of the plates to different beam intensities while using hybrid Boron Carbon foils [38]. In this graph only the case with BSE3 and BSW4 at nominal current (3092 A) is represented. From the image we can appreciate that in all the cases the signal is mainly on the H0R plate. A non negligible signal can also be found in the HMR plate. In order to certify which kind of particle was reaching each plate some of these measurements were also taken with a different value of the BSWs' current. The only difference found between the measurements was the signal measured by the HMR plate. This means the signals on the H0L, H0R and HML plates are generated by H^0 whereas the signal on the HMR plate is generated due to H^- particles.

Once again, we can find two different families of measurements corresponding to the two different models of the electronics tested. To be consistent with the calibration factor calculated on the previous section, the rest of the results will only include the data from the corresponding version of the electronics (points around $0.8 \cdot 10^{-9}$).

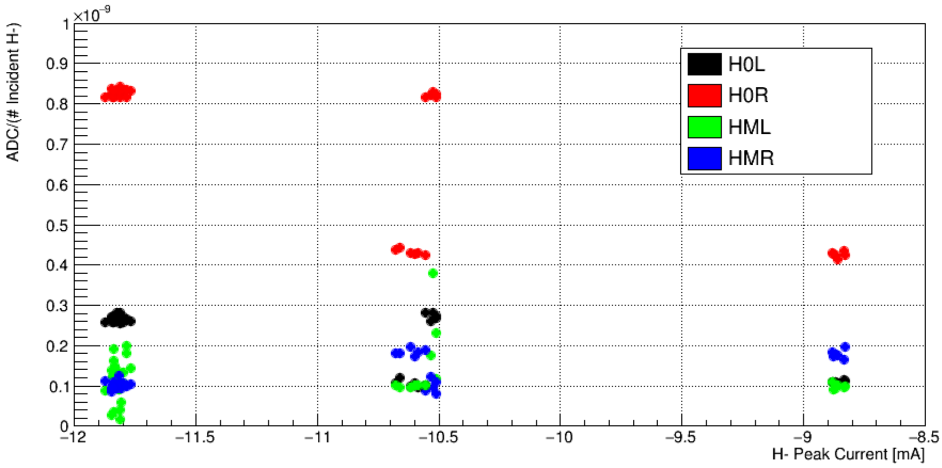

Figure 33: Signal read out by different plates normalized by number of charges measured with BCT.1043. Each color correspond to each one of the plates. Measurements taken using a hybrind Boron-Carbon Foil.

$k = 6.807 \cdot 10^{-7}$ was the value of the calibration factor found on the previous section. This value relates the signal coming from each plate, in ADC units, with the total number of particles reaching each plate. Using this value we can calculate the total number of incident particles. This value can be compared with the number of charges measured by the BCT before the stripping foil. The ratio between these two values will give the stripping inefficiency of the corresponding stripping foil. For doing those calculations, an important detail has to be taken into account. k was calculated with an incident H^- beam. In order to be able to use this calibration factor we have to take into account the differences on the signal produced by an H^0 or an H^- particle.

If we go back a couple of pages, Table 10 shows the relative difference between signals due to H^0 and H^- particles. This difference being 2.328 with secondary emission and 2.031 without secondary emission. In our case a relative high magnetic field was present during the measurements so we can assume SEE was suppressed. If we want to use the k factor for a signal produced by H^0 particles, it should be divided by a factor 2.031 as the signal produced by H^- is twice the one produced by H^0. Formula 32 summarizes how the stripping inefficiency is calculated using the signal measured by the plates and the calibration factor.

$$SI = \frac{\frac{1}{k} \cdot (2 \cdot ADC_{H0L} + 2 \cdot ADC_{H0R} + 2 \cdot ADC_{HML} + ADC_{HMR})}{\#ChargesBCT.1043} \tag{32}$$

If we follow the procedure explained on the previous paragraphs we obtain a stripping inefficeincy of 0.234% for stripping foil 6 and 0.369% for stripping foil 5, see Table 11. Another method to measure the stripping inefficiency is also available. Along these pages we've been talking about BCT.1043 which allowed to measure the number of particles before the stripping foil. Another BCT is placed downstream the stripping foil, that is BCT.1073. Dividing the number of charges measured by the BCT downstream and the BCT upstream the stripping foil, we are able to calculate the stripping efficiency. On the previous case we calculated a stripping efficiency of 98.61% for SF 5 and 98.75% for SF6, or what is the same, a stripping inefficiency of 1.389% for SF5 and 1.243% for SF6.

A non negligible difference appears when measuring the stripping inefficiency by these two different methods. The reason for this discrepancy can be explained if we include in our analysis the possible lost of protons between the two BCTs. Let's give this a little more of context.

Description	**Foil Number**	**Size [mm]**
XCF-200, arc evaporated amphous Carbon, collodion caoated	1-4	32 x 68
DLC-23-1000-S, Diamond-like Carbon, boron doped 10%	2-3	32 x 68
HBC, Hybrid type Boron mized Carbon	5-6	21 x 68

Table 11: Characteristics of the different foil types used. From [38]

6 different stripping foils were tested. In Table 11 we can find a summary of the characteristics of these different stripping foils. For the first 4 stripping foils no signal was appreciated on the plates, or the signal was too small to clearly differentiate it from noise. Nevertheless, in those cases also a stripping inefficiency of ≈ 1% is measured by the BCTs. This could be explained if some protons were lost before reaching the BCT downstream the stripping foil. If that was the case the missing particles could not be counted as stripping inefficiency as they have been correctly stripped. If in all the cases we consider that 1% of the particles are going to be protons lost between the two BCTs, the stripping inefficiency calculated with the BCTs would be ≈ 0.389% for SF 5 and ≈ 0.243% for SF 6.

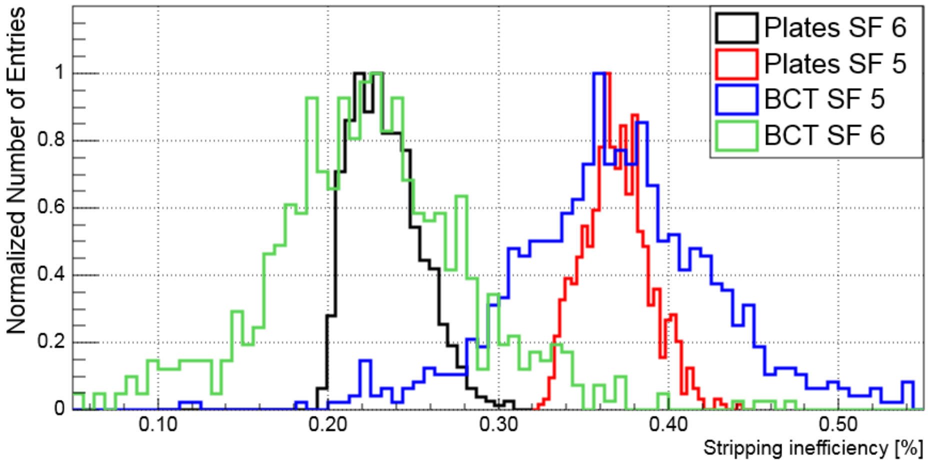

Figure 34: Distribution of the stripping inefficiency as measured by the $H^0 H^-$ monitor and by the BCTs over about 700 LINAC4 pulses, with two different Hybrid Boron Carbon stripping foils.

Figure 34 is a quantification of the previous explanation. The red and black lines correspond to the histograms of the stripping inefficiency calculated with the plates for SF 6 and SF 5 respectively. Alike, the green and blue curves are the histograms of the stripping inefficiency calculated using the BCTs. All these histograms have been normalized by the total number of entries so measurements with both stripping foils can be compared.

All the results presented in this chapter where calculated using the signal from the continuous monitoring system. The interlock signal was also available. A clear linear dependence with beam intensity was observed over a large intensity range [39]. Nevertheless, no further tests were done to study in detail the interlock functionality.

The Half Sector Test stopped activities on the 6th of April 2017 after around 3 months of operation. This period was very useful to verify the performance of the H^0H^- beam current monitors. Nevertheless, this period was not enough to fully establish the absolute accuracy of the device, study in detail the interlock functionality or test the final version of the electronics. Ways to complete these studies are now being investigated.

Conclusions

The first month of the work at CERN was dedicated to understand the particle interaction with matter, with emphasis on Secondary Electron Emission phenomena. Afterwards it was possible to learn how Secondary Emission Monitors (SEM) use this effect for transverse beam monitoring (Chapter 2). SEM comprehend an assortment of different types of detectors. In this thesis SEM grids and Wire Scanners are the ones presented with more detail even though a bunch of other types of detectors also exist (Chapter 3).

Due to their intercepting nature, SEM detectors have an effect on the beam (emittance blow up). At the same time the beam has an effect of them (Signal generation, thermal fluctuations, etc.). Several python routines were implemented in order to simulate, among others, the previous phenomena, that is, emittance growth, signal generation and temperature evolution of the monitors (Chapter 4). If not indicated otherwise, the results presented in this thesis have been calculated with the aforementioned routines. It is foreseen that user friendly versions of these programs will be available after August 2017 if no other priorities come up.

Even if it was not with a lot of detail, softwares like Fluka and CST Particle studio were learned and used. Some results calculated with these programs can be found along the pages.

Beam profile measurements where taken with SEM grids and Wire scanners although finally these measurements where not included on this document. Neither emittance measurements (Chapter 5) nor H^0H^- calibration (Chapter 6) were included on the initial planning of the work. Nevertheless, the need for these measurements and its relevance were reasons enough to include them.

Special attention should be given to references [37], [38] and [39]. These three articles were published during May 2017 for IPAC conference in Copenhagen, Denmark. Concretely, [37] includes general information about the Half Sector Test and the measurements performed since it firstly received beam on October 2016. [38] presents detailed information about the stripping foil units tested in the HST as well as their operational experience. Finally, [39] includes a summary of the beam instrumentation available in LINAC4 and PSB HST as well as a summary of the results presented in Chapter 6.

References

[1] L. Arnaudon, et al. *Linac4 Technical Design Report.* CARE-Note-6006-22-HIPPI, CERN, Switzerland.

[2] NIST, National Institute of Standars and Technology. Physical Meas. Laboratory.

[3] A. Missimiliano Schiavi, *Study of Laser produced Plasmas by X-Ray and Proton Radiography*, Plasma Physics Group, PhD, London,2003.

[4] D.E. Groom, et al., *Muon Stopping Power and range Tables 10 MeV- 100TeV*, Atomic Data and Nuclear Data Tables, Vol 76., No, 2, July 2001.

[5] K. Nakamura et al. (PDG), *Passage of particles through matter*, February 16, 2012, JP G 37 075021.

[6] W. Frass,*Passage of particles through matter*, Oxford physics 2009.

[7] D. Krammer, *Design and Implementation of a Detector for High Flux Mixed Radiation Fields*, Department of physics, University of Livec, Phd, Czech Republic, 2008.

[8] D. Hasselkamps, et al. *Ion induced secondary electron spectra from clean metal surfaces*, Nuc. Instrum. and Methods Phys. Res. B 18 (1987) 561.

[9] http://www.fluka.org/fluka.php

[10] G.Lakits, et al., *Statistics of ion-induced electron emission from a clean metal surface*, American Institute of physics, 22 June 1989.

[11] E. Borokovsky, et Al. *The secondary-electron yield measured for 5-24 MeV protons on aluminium-oxide and gold targets*, Nuclear Instr. and Methods in Physics Research, 1988.

[12] P.Thieberger, et al. *Secondary-electron yield and their dependence on the angle of incidence on stainless-steel surfaces for three energetic beams*, Physicak Review, Volume 61, 04291

[13] http://www.cloudylabs.fr/wp/nombre-de-delta-ray/

[14] Allan J. et al. *Backscattering and secondary electron emission from metal targets of various thiknesses*, Washinton, D.C., April 1965.

[15] V.L. Highland. *Some practical remarks in multiple scattering*, Nucl. instr. and meth, Vol.129 p.497, 1975.

[16] G.R. Lynch and O.I. Dahl. *Approximation to multiple Coulom scattering*, Nucl. instr. and meth, Vol. B58, p.6, 1990.

[17] U.Raich, *Beam Diagnostics*, CERN, Geneva, Switzerland.

[18] F.Roncarolo, et al. *H^- and H^0 beam current monitor electronics.*, PSB-BC-ES-0001, CERN, Geneva, Switzerland.

[19] L.Wang, et al. , *Suppression of secondary emission in a magnetc field using a swatooth and isosceles triangle surface*, SLAC, Menlo Park, CA, USA.

[20] M. Sapinski, *Model of Carbon Wire Heating in Accelerator Beam*, CERN, Geneva, Switzerland, 2008.

[21] Gorazd Planinšič, *Thermionic Emission*,University of Ljubljana, Department of physics, April, 2008.

[22] M. Möser, *Fractography with the SEM (Failure Analysis)*, 2007.

[23] F. Roncarolo, *Accuracy of Transverse Emittance Measurements of the CERN Large Hadron Collider*, Ecole Polytechnique federale de Lausanne, PhD Lausanne, 2005

[24] J. Buon, *Beam Phase space and Emittance*, LAL, 91405 Orsay, France

[25] F.Roncarolo, et al., *Accuracy determination of the CERN LINAC4 emittance measurements at the test bench for 3 and 12 MeV*. CERN Geneva Switzerland. 2010.

[26] J. Lettry, et al. , *LINAC4 H* ion sources*, Review of scientific instruments 87,02B139, 2016.

[27] M. Lutz, *CERN LINAC4 - The Space Charge Challenge*, University of Berlin, PhD, 2013.

[28] U. Raich, et al., *Commisioning of the CERN LINAC4 wire scanner, wire grid and slit-grid monitors at 3 and 12 MeV*, Proceedings of Linac, 2014, Geneva, Switzerland.

[29] B. Cheymol, et al., *Scattering of H^- Stripped Electrons from sem grids and wire scaners at CERN LINAC4* , Proceedings of LINAX2012, Tel-Aviv, Israel.

[30] https://www.cst.com/products/cstps

[31] B. Cheymol, et al. , *Comissioning of the LINAC4 ion source transverse emittance meter*, CERN-BE-2010-014 BI.

[32] F. Roncarolo, et al., *Effect of H^- stripped electrons on the LINAC4 profile measurements*, CERN-ACC-NOTE-2014-008 TECH

[33] C.Hojvat, et al., *The multiturn charge exchange injection system for the fermilab booster accelerator*, IEE Transactions on Nuclear Science, Vol. NS-26, N° 3, June 1979.

[34] T. Kawakubo, et al., *The H^- exchange injection system in the booster of the KEK 12 GeV proton Synchrootron*, National laboratory for high energy Physics, Japan.

[35] V. Lienchtenstein, *Carbon Stripper Foils- Preparation and quality*, Kurchatov Institute, 123182 Moscow, Russia.

[36] Huang Ming-Yang, et al., *The effects of injection beam parameters and foil scattering for CSNS/RCS*, institute of high energy physics, China, 2012.

[37] B. Mikulec, et al. *Commissioning and results of the half-sector test installation with 160 MeV H^- Beam from LINAC4* , CERN, Geneva Switzerland. .

[38] C. Bracco, et al. *Commissioning of the stripping foil units for the upgrade of the PSB H^- injection system*, CERN, Geneva, Switzerland.

[39] F. Roncarolo, et al. ,*Beam instrumentation for the CERN LINAC4 and PSB Half Sector Test*, CERN, Geneva, Switzerland